Journal Code:				Article ID				Dispatch: 27.09.14	CE: Kate Cadimas
N	M	E		4	7	8	8	No. of Pages: 25	ME:

INTERNATIONAL JOURNAL FOR NUMERICAL METHODS IN ENGINEERING
Int. J. Numer. Meth. Engng (2014)
Published online in Wiley Online Library (wileyonlinelibrary.com). DOI: 10.1002/nme.4788

RESEARCH ARTICLE

Accuracy of three-dimensional analysis of regularized singularities

Elena Benvenuti[1,*,†], Giulio Ventura[2], Nicola Ponara[1] and Antonio Tralli[1]

[1]*ENDIF, University of Ferrara, Via Saragat 1, 44122 Ferrara, Italy*
[2]*DISEG, Politecnico di Torino, Corso Duca degli Abruzzi 24, 10129 Torino, Italy*

SUMMARY

In computational mechanics, the quadrature of discontinuous and singular functions is often required. To avoid specialized quadrature procedures, discontinuous and singular fields can be regularized. However, regularization changes the algebraic structure of the solving equations, and this can lead to high errors. We show how to acquire accurate and consistent results when regularization is carried out. A three-dimensional analysis of a tensile butt joint is performed through a regularized extended finite element method. The accuracy obtained via Gaussian quadrature is compared with that obtained by means of CUBPACK adaptive quadrature FORTRAN tool. The use of regularized functions with non-compact and compact support is investigated through an error evaluation procedure based on the use of their Fourier transform. The proposed procedure leads to the remarkable conclusion that regularized delta functions with non-compact support exhibit superior performance. Copyright © 2014 John Wiley & Sons, Ltd.

Received 24 January 2014; Revised 21 May 2014; Accepted 14 August 2014

KEY WORDS: singularities; regularization; 3D quadrature; XFEM; fourier transform

1. INTRODUCTION

Quadrature of discontinuous and singular integrands is a challenging issue in computational mechanics. However, it cannot be handled by means of standard quadrature procedures, unless sharp discontinuities are regularized. Because regularization of sharp discontinuities might generate excessive errors, we show under which conditions it can be effective. For this purpose, Gaussian quadrature and adaptive quadrature are applied to a regularized variant of the extended finite element method (XFEM). A novel error evaluation procedure based on the Fourier transform of the regularized functions is used to compare non-compact and compact support regularized functions. The proposed procedure leads to the worth noting conclusion that regularized delta functions with non-compact support should be used to have robust and effective results.

Singular and highly localized fields occur in several computational mechanics fields, such as in applications of the vortex method [1], the immersed boundary method [2, 3], the phase-field method [4, 5], in advection-diffusion problems [6, 7], electronic structure calculations [8], and in the modeling of plastic hinges in beam elements [9]. In the context of the finite element modeling, quadrature of terms containing discontinuous and singular functions is performed by subdividing the elements crossed by discontinuities in quadrature sub-domains [10, 11] or, alternatively, by making use of adaptive quadrature [8, 12]. Subdivision into quadrature sub-domains can be cumbersome in the multidimensional case. Quadrature in the multidimensional case was studied by [13] among the first. They proposed an algorithm for the recursive subdivision of one cube into n-cubes until the

*Correspondence to: Elena Benvenuti, Engineering Department, University of Ferrara.
†E-mail: elena.benvenuti@unife.it

error over each subdivision is smaller than a prescribed tolerance. Recently, improving the scheme [13], an adaptive procedure was proposed [8], where a tensor product rule with eight nodes in all directions is used to estimate the local integration error. If the error is larger than a prescribed tolerance, then the element is subdivided into cells and the adaptive integration is performed over each cell recursively. A Gaussian-like quadrature rule was constructed in two-dimensions on the basis of a point-elimination algorithm for the final quadrature scheme to have the minimal number of Gauss points [14]. Alternatively, a technique based on the replacement of the Heaviside function with equivalent polynomial functions such that their integral gives the exact values of the discontinuous/non-differentiable function integrated on subcells was proposed [15]. As the polynomial is defined in the whole element domain, Gaussian quadrature can be employed, and no quadrature sub-domains are required. In three-dimensions, an adaptive tree-based adaptive approach to a variant of the discontinuous Galerkin method that is characterized by discontinuous enrichments of the polynomial basis has been developed in [12].

The standard mathematical approach to regularization consists in replacing singular and discontinuous functions with a regularized delta function and a regularized Heaviside function, respectively, whose support is governed by a length parameter ρ. The only requisite is that, for vanishing ρ, the original singular and discontinuous functions are recovered. As known, regularization introduces approximations in the computation. The interpolation properties of the discrete form of delta function were studied by Beyer and Leveque [3] in the framework of Peskin's immersed boundary method [2]. They showed that the numerical error related to the replacement of a singular integrand with a regularized one depends on the number of continuous moment conditions that are satisfied [3]. Tornberg and coworkers [16, 17] gave fundamental contributions to the study of the discretization error associated with regularization. They analyzed the case of regularizations with narrow support. For instance, they showed that, when the regularization is well resolved on the quadrature grid, the total error can be split into the sum of the analytical and the quadrature error. Fast algorithms for the solution of integral equations with singular and localized kernels were proposed in references [18, 19].

The level set method [20] is a highly successful computational technique for tracking the spatial evolution of three-dimensional surfaces. An attractive feature is that interfaces are implicitly described by this method and do not need to be parameterized. The use of the level set method [20] leads to a straightforward extension of the regularized Heaviside and delta functions to the multi-dimensional case. Unfortunately, regularization procedures based on the extension of the level set signed distance function to the multi-dimensional case may lead to errors that do not decrease for decreasing mesh size, when compact support regularization is adopted. The problem with extending the regularization to higher dimensions using the closest distance to the interface is that the aforementioned moment conditions are no longer valid for any position of the discontinuity. More recently, it has been shown [21] that the approximation of a one-dimensional delta function extended to higher dimensions by a distance function can be made accurate with non-compact support regularized functions. The price to pay is that the support is wider. If the regularized function has a non-compact support, then it is infinitely differentiable and the regularity of the regularized function will no longer affect the numerical error.

In this paper, we investigate the three-dimensional finite element modeling of problems where singular strain fields arise because of the presence of discontinuities in the displacement field. We compare the accuracy and the robustness of the results, when compact and non-compact support regularizations are performed. We formulate the problem in the framework of the XFEM [10, 11, 22–24]. XFEM is a powerful technique for modeling engineering problems characterized by discontinuous and singular functions. It is based on incorporating functions reproducing features of the solution, such as discontinuities or singularities. Our approach is based on the regularized variant of the XFEM, first proposed by the authors in [25]. It is suitable for modeling thin and thick cohesive interfaces and strain localization without the need of sub-quadrature subdivision [26–28]. Regularized XFEM is also an effective alternative to nonlocal and cohesive crack-models [29–31]. Its mechanical consistency has been thoroughly discussed in [27, 28]. One of the advantages of adopting this regularized XFEM is that blending [32, 33] is not required. Whereas kinematics is regularized analogously to other approaches based on the regularization of the Heaviside and delta

DOI: 10.1002/nme

functions [7–9, 34, 35], the strain fields, the constitutive modeling, and the adopted variational formulation are different.

The original contribution of this paper concerns the novel use of the Fourier transform for the evaluation a priori of the robustness of the regularization procedure. After an introduction to the regularization of singular functions in the level set context in Section 2, the accuracy of the procedure based on the replacement of the singular delta function with a regularized delta function is discussed and formulated by means of the moment conditions [3] in Section 3. The moment conditions are formulated in terms of the Fourier transforms of the regularized delta functions in Section 4.2. In particular, the class of regularized delta functions considered in the present paper are more general than those studied by [21]. The advantages in using the Fourier transform are several. First, the relationship between the regularization support width of the regularized delta function and the expected accuracy is put into evidence by the use of the similarity rule of the Fourier transforms as addressed in Section 4.3. Furthermore, the choice of the regularized delta function follows by simply looking at the support width and the type of decaying behavior of the corresponding Fourier transform. The procedure highlights that the use of regularized delta functions with compact support can lead to loss of convergence. As a computational model, the regularized XFEM approach addressed in Section 5 is adopted. In Section 6, the structural analysis of a tensile butt joint where the joint is slanted with respect to the loading direction is studied. In particular, the bell function, with compact support, and the Laplacian function, with non-compact support, have been adopted. The aim is to assess the accuracy of the stress evaluation of the structural example (Section 6.2). A critical comparison follows in Section6.3.

2. REGULARIZATION IN THE LEVEL SET CONTEXT

In this section, we first introduce a certain class of regularized delta functions in the level set context. Then, we formulate the moment conditions governing the error related to the replacement of a singular integrand with a regularized one.

2.1. Regularized delta functions

Let the volume V be divided into V_1 and V_2 by the interface S. At any point $\mathbf{x} \in S$, the interface is characterized by the normal vector $\mathbf{n}(\mathbf{x})$. The position of S is implicitly defined by means of the signed distance function $d(\mathbf{x})$ with respect to S [20], defined as $d(\mathbf{x}, S) = \text{dist}(\mathbf{x}, S)$ if $\mathbf{x} \in V_1$, and $d(\mathbf{x}, S) = -\text{dist}(\mathbf{x}, S)$ if $\mathbf{x} \in V_2$.

Our purpose is to numerically integrate terms containing singular functions such as

$$\mathcal{I}_\delta = \int_V \delta(d(\mathbf{x}), S)\, f(\mathbf{x})\, dV. \tag{1}$$

To avoid specialized quadrature procedures, we want to replace the delta function δ by a regularized version δ_ρ

$$\delta_\rho(d) = \frac{1}{\ell_\rho}\varphi_\rho(d), \qquad \underline{\lim}_{\rho\to 0}\delta_\rho(t) = \delta(t), \tag{2}$$

where ℓ_ρ is a normalization length, which depends on the type of the regularized delta function, and $\underline{\lim}$ indicates weak convergence [36]. In particular, φ_ρ is a smooth delta function depending on a length ρ such that

$$\int_{-\infty}^{\infty} \delta_\rho(t)\, \mathrm{d}t = \frac{1}{\ell_\rho}\int_{-\infty}^{\infty} \varphi_\rho(t)\, dt = 1. \tag{3}$$

Examples of regularized delta functions with compact support are the *hat function*

$$\varphi_\rho^H(d) = \begin{cases} 1 - \frac{|d|}{\rho} & \text{if } |d| \leqslant \rho, \\ 0 & \text{otherwise,} \end{cases} \tag{4}$$

DOI: 10.1002/nme

and the *bell functions*

$$\varphi_\rho^B(d) = \begin{cases} \left(1 - \frac{d^2}{\rho^2}\right)^n & \text{if } |d| \leqslant \rho, \\ 0 & \text{otherwise,} \end{cases} \tag{5}$$

with $n = 2,\ 4$. Examples of regularized delta functions with non-compact support are the Laplacian regularized delta function

$$\varphi_\rho^L(d) = e^{\frac{-|d|}{\rho}}, \tag{6}$$

and the *Gauss function*

$$\varphi_\rho^G(d) = e^{-\frac{d^2}{\rho^2}}. \tag{7}$$

Other expressions of the regularized delta function are eligible as well [34, 37].

3. ACCURACY AND MOMENT CONDITIONS

According to [3], we consider a one-dimensional domain where a regular grid of evaluation points $x_j = j\,h$, with $j \in \mathbb{Z}, \mathbb{Z}$ being the set of the integer numbers. The integral of the smooth function f multiplied by the delta function δ is approximated as

$$\int_{-\infty}^{\infty} \delta(x - x^*)\, f(x)\, dx \approx h \sum_{j\in\mathbb{Z}} f(x_j)\delta_\rho(x_j - x^*), \tag{8}$$

where δ_ρ is a regularized delta function. As $f(x)$ is differentiable by hypothesis, $f(x_j)$ can be developed in a Taylor series about the point x^* as follows

$$f(x_j) = f(x^*) + \sum_{r=1}^{\infty} \frac{1}{r!} f^r(x^*)(x_j - x^*)^r, \tag{9}$$

where f^r represents the r-order derivative of f. Hence, the error corresponding to the approximation (8) can be expressed as

$$\begin{aligned} \mathcal{E} &= \int_{-\infty}^{\infty} f(x)\delta(x - x^*)\, dx - h \sum_{j\in\mathbb{Z}} f(x_j)\delta_\rho(x_j - x^*) = \\ &= f(x^*) - h\, f(x^*) \sum_{j\in\mathbb{Z}} \delta_\rho(x_j - x^*) - \sum_{r=1}^{\infty} \frac{1}{r!} f^r(x^*)\, h \sum_{j\in\mathbb{Z}} (x_j - x^*)^r \delta_\rho(x_j - x^*). \end{aligned} \tag{10}$$

The first and second terms in (10) cancel out if the *mass or normalization condition*

$$h \sum_{j\in\mathbb{Z}} \delta_\rho(x_j - x^*) = 1 \tag{11}$$

is satisfied. If the mass condition (11) holds, then the interpolation error $\mathcal{E}$ (10) will be of the order $\mathcal{O}(h)$ for vanishing h. For the regularized delta function which vanishes for $|x| > M_x$, where M_x is a certain decaying distance, the third term in (10) is $\mathcal{O}(h^r)$ for vanishing h [3].

We can thus summarize the above results by stating that if the *moment conditions*

$$h \sum_{j\in\mathbb{Z}} (x_j - x^*)^r \delta_\rho(x_j - x^*) = \begin{cases} 1 \text{ for } r = 0 \\ \\ 0 \text{ for } r = 1, 2, \ldots, q-1 \end{cases} \tag{12}$$

DOI: 10.1002/nme

are fulfilled, then the error (10) is

$$\mathcal{E} = \int_{-\infty}^{\infty} f(x)\delta(x - x^*)\, dx - h \sum_{j\in\mathbb{Z}} f(x_j)\, \delta_\rho(x_j - x^*) = \mathcal{O}(h^q), \tag{13}$$

for vanishing h.

4. ACCURACY AND FOURIER TRANSFORMS

The relationship between the evaluation of the accuracy of the integration of a singular function and the use of the Fourier transform is investigated. In Section 4.1, we recall some basic properties of the Fourier transform, which will be useful for the subsequent developments. Following [38] and [21], in Section 4.2, the moment conditions formulated in Section 3 are rewritten in terms of the Fourier transform of the regularized delta function. In this way, the relationship between the width of the regularized delta function support and the expected accuracy becomes evident. Moreover, the computation of the moment conditions, which is not always feasible, is not required. As shown in Section 4.3 and Section 4.4, the choice of the regularizing delta function follows by simply looking at the support width and the type of decaying behavior of the corresponding Fourier transform. The truncation error associated with the use of regularized delta functions with non-compact support is investigated in Section 4.5 [38] proved that the moment conditions (12) hold also in the multidimensional case if the level set definition (2) of the regularized delta function is assumed.

4.1. Some classical results on the Fourier transforms

To discuss the accuracy of the quadrature procedure in the multidimensional case, we exploit the results recently obtained by [21] based on the Fourier transforms properties. We introduce the Fourier transform $\hat{f}$ of a generic function f as

$$\hat{f}(\kappa) = \int_{-\infty}^{\infty} e^{-2\pi\, i\, \kappa\, x}\, f(x)\, \mathrm{dx}. \tag{14}$$

A synoptic table of the Fourier transforms of some relevant regularized delta functions, without the normalization length, is reported in Table I. T1

We ~~need to be precise with~~ the similarity rule governing the Fourier transforms of regularized delta functions whose argument is not t but t/ρ. The similarity rule of the Fourier transform states that if $\hat{f}(\kappa)$ is the Fourier transform of $f(t)$, then the Fourier transform of $f(a\,t)$ Q1

$$f(ax) \to \hat{f}\Big|_{ax} = \frac{1}{a}\hat{f}\left(\frac{\kappa}{a}\right), \tag{15}$$

where $a > 0$ is a constant. In Equation (15), the symbol $\to$ indicates the operator mapping a function into its Fourier transform. By the similarity rule (15), setting $a = 1/\rho$, we obtain the Fourier transforms of the regularized delta functions which depend on the argument t/ρ.

$$f\left(\frac{x}{\rho}\right) \to \hat{f}\Big|_{x/\rho} = \rho\hat{f}(\rho\kappa). \tag{16}$$

Table I. Elementary Fourier transforms.

f	$\hat{f}$
$\max(0, 1 - \lvert t\rvert)$	$(\sin(\pi\kappa)/(\pi\kappa))^2$
$\max(0, 1 - t^2)$	$(4\sin\kappa - 4\kappa\cos\kappa)/\left(\sqrt{(2\pi)}\kappa^3\right)$
$e^{-a\lvert t\rvert}$	$2a/(a^2 + 4\pi^2\kappa^2)$
$e^{-\pi t^2}$	$e^{-\pi\kappa^2}$

DOI: 10.1002/nme

Furthermore, for a rapidly decreasing function φ, the Poisson summation formula states that

$$\sum_{x\in\mathbb{Z}} \varphi(x) = \sum_{\kappa\in\mathbb{Z}} \hat{\varphi}(\kappa). \tag{17}$$

By the similarity rule (15), for the regularized delta functions considered here, Equation (17) becomes

$$\sum_{x\in\mathbb{Z}} \varphi_\rho\left(\frac{x}{\rho}\right) = \rho \sum_{\kappa\in\mathbb{Z}} \hat{\varphi}(\rho\,\kappa). \tag{18}$$

Noteworthy, according to the similarity rule, making a function wider or narrower makes its Fourier transform narrower and taller or wider and shorter, respectively, always conserving the area under the transform. The Fourier transforms of the most relevant ρ-dependent regularized delta functions are shown in Table II.

4.2. *Moment conditions and Fourier transforms*

According to [38], the discrete moment order of the one-dimensional delta function approximation determines the order of approximation related to the replacement of the singular delta function with the regularized delta function. We next establish the moment conditions for a wide range of positions of the singularity over a regular grid.

Multidimensional Moment conditions: *Assume a regular grid in one dimension with grid points* $x_j = j\,h$, $j \in \mathbb{Z}$, $x^* = x_n + p\,h$ *with* $0 < p < 1$ *and* $n \in \mathbb{Z}$. *Consider a* δ_ρ *general approximation of the type* $\delta_\rho = \ell_\rho^{-1}\varphi_\rho(t/\rho)$, *where* $\rho = M\,h$ *and the normalization length is* $\ell_{rho} = L\,\rho$, *with* M, $L > 0$. *If* $\hat{\varphi}_\rho(\kappa)$ *has compact support on* $[-\beta, \beta]$, and

$$\left.\frac{\partial^r \hat{\varphi}_\rho(\kappa)}{\partial \kappa^r}\right|_{\kappa=0} = \begin{cases} L, & \text{for } r = 0, \\ 0, & \text{for } 1 \leqslant r < q, \end{cases} \tag{19}$$

then for all $M \geqslant \beta$ *the* δ_ρ *approximation satisfies* q *discrete moment conditions.*

The result (19) is more general than that stated in [21], because it holds also for general normalization lengths, whereas in [21] only the case of normalization length equal to ρ is considered.

A proof of Equations (19) follows. The multidimensional version of the moment conditions for a level set dependent regularized delta function can be expressed as

$$\mathcal{M}_r(\delta_\rho, x^*, h) = h \sum_{j\in\mathbb{Z}} \frac{1}{L\,\rho}\varphi_\rho\left(\frac{x_j - x^*}{\rho}\right)(x_j - x^*)^r, \tag{20}$$

where $\ell_\rho = L\,\rho$ with $L > 0$. Let us set

$$f_{r\rho}(x) = \frac{1}{\ell_\rho}\varphi_\rho\left(\frac{x}{\rho}\right)x^r = \frac{1}{L\,\rho}\varphi_\rho\left(\frac{x}{\rho}\right)x^r. \tag{21}$$

Table II. Elementary Fourier transforms after application of the similarity rule, $\hat{f}_\rho(t/\rho) = \rho\hat{f}_\rho(t\rho)$.

f_ρ	$\hat{f}_\rho$
$\max(0, 1 - \lvert t\rvert/\rho)$	$\rho(\sin(\pi\rho\kappa)/(\pi\rho\kappa))^2$
$\max(0, 1 - (t/\rho)^2)$	$\rho(4\sin(\rho\kappa) - 4\rho\kappa\cos(\rho\kappa))/\left(\sqrt{(2\pi)}(\rho\kappa)^3\right)$
$e^{-\lvert t\rvert/\rho}$	$2\rho/(1 + 4\pi^2\rho^2\kappa^2)$
$e^{-\pi(t/\rho)^2}$	$\rho e^{-\pi(\rho\,\kappa)^2}$

DOI: 10.1002/nme

The Fourier transform of Equation (21) is such that

$$f_{r\rho}(x) = \frac{1}{L\,\rho}\varphi_\rho\left(\frac{x}{\rho}\right) x^r \quad \rightarrow \quad \hat{f}_{r\rho}\Big|_x = \frac{\rho}{L\,\rho}\frac{1}{(-2\pi\,i)^r}\frac{\partial^r}{\partial\kappa^r}\hat{\varphi}_\rho(\rho\kappa). \tag{22}$$

where $\hat{f}_{r\rho}\Big|_x$ indicates the Fourier transform of f as a function of x, to be kept distinguished from $\hat{f}_{r\rho}\Big|_{x-x^*}$, the Fourier transform of $f_{r\rho}(x-x^*)$, being

$$f_{r\rho}(x-x^*) = \frac{1}{L\,\rho}\varphi_\rho\left(\frac{x}{\rho}\right) x^r \quad \rightarrow \quad \hat{f}_{r\rho}\Big|_{x-x^*} = e^{-2\pi\,i\,\kappa\,x^*}\frac{\rho}{L\,\rho}\frac{1}{(-2\pi\,i)^r}\frac{\partial^r}{\partial\kappa^r}\hat{\varphi}_\rho(\rho\kappa). \tag{23}$$

By the Poisson summation formula (17), the relationship

$$\sum_{j\in\mathbb{Z}} h\varphi_\rho(h\,j) = \sum_{\kappa\in\mathbb{Z}}\hat{\varphi}_\rho\left(\frac{\kappa}{h}\right) \tag{24}$$

holds. After setting $x^* = p\,h$, the moment conditions write

$$\mathcal{M}_r(\delta_\rho, p\,h, h) = \sum_{\kappa\in\mathbb{Z}} e^{-2\pi\,i\,\kappa\,p}\frac{1}{L}\frac{1}{(-2\pi\,i)^r}\frac{\partial^r}{\partial\kappa^r}\hat{\varphi}_\rho\left(\frac{\rho\kappa}{h}\right). \tag{25}$$

By exploiting Equations (24) and (23), Equation (20) has the following expression

$$\mathcal{M}_r(\delta_\rho, p\,h, h) = \sum_{\kappa\in\mathbb{Z}} e^{-2\pi\,i\,\kappa\,p}\frac{1}{L}\frac{1}{(-2\pi\,i)^r}\frac{\partial^r}{\partial\kappa^r}\hat{\varphi}_\rho(M\kappa), \tag{26}$$

where $\rho = M\,h$ was set. Finally, the multidimensional version of the discrete form(26) of the moment conditions for a level set dependent regularized delta function can be formulated as

$$\mathcal{M}_r(\delta_\rho, p\,h, h) = \frac{1}{(-2\pi\,i)^r}\frac{1}{L}\left[\frac{\partial^r\hat{\varphi}_\rho(M\,\kappa)}{\partial\kappa^r}\Big|_{\kappa=0} + \sum_{\kappa\in\mathbb{Z},\kappa\neq 0} e^{-2\pi\,i\,\kappa\,p}\frac{\partial^r\hat{\varphi}_\rho(M\,\kappa)}{\partial\kappa^r}\right]. \tag{27}$$

From Equation (27), it can be drawn that the second term at the right hand side of Equation (27) vanishes when

- $\hat{\varphi}_\rho$ has compact support on $(-\beta,\beta)$ for any $M > \beta$;
- $\hat{\varphi}_\rho$ is a periodic function for certain particular M;
- $\hat{\varphi}_\rho$ does not have a compact support, but it decays fast beyond $\pm\beta$: once fixed a certain tolerance, it can be truncated outside the interval $[-\beta,\beta]$.

In particular, if $\hat{\varphi}_\rho$ has compact support on $(-\beta,\beta)$ and the conditions (19) on the derivatives are satisfied for all $M \geqslant \beta$, the regularized delta function $\delta_\rho = \ell^{-1}\varphi_\rho$ *exactly* satisfies q discrete moment conditions (27).

When the Fourier transform is non-compact and satisfies conditions (19) up to order q, then q discrete moment conditions (27) are satisfied in an approximate way with an error which decreases for increasing width of the truncated support $[-\beta,\beta]$.

As proven in [17, 38], compact support functions such as the hat function or the cosine function fail to satisfy the mass condition (11) for any non integer M. In the two-dimensional and the three-dimensional case, this limitation becomes more evident. This is because of the number of quadrature points within the support is not constant, but it changes depending on the discretization and the geometry of the interface with respect to the mesh.

DOI: 10.1002/nme

4.3. Practical examples of Fourier transforms

Interestingly, the Fourier transform of a compact support regularized delta function such as the linear hat function (4)

$$\hat{\varphi}_\rho^H(\kappa) = \frac{\sin^2(\pi\,\kappa)}{\pi^2\,\kappa^2} \tag{28}$$

has an oscillatory character, as shown in Figures 1a and 1b for $\rho/W = 2/10$ and $\rho/W = 5/10$, respectively. Hence, it does not possess a compact support and cannot be truncated. The mass condition for this case is

$$M_0\left(\delta_\rho^H, x^*, h\right) = 1 + \sum_{\kappa\in\mathbb{Z},\kappa\neq 0} e^{-2\pi\,i\,\kappa\,p}\frac{\sin^2(\pi\,M\,\kappa)}{\pi^2\,M^2\,\kappa^2}, \tag{29}$$

where $L = 1$. The second term in the mass condition (29) vanishes for any dilation x^* when $\sin(\pi M\kappa) = 0$ for all $\kappa \in \mathbb{Z}, \kappa \neq 0$, hence for integers $M \geqslant 1$. Thus, no β exists such that for any $M > \beta$ the mass condition is satisfied. Furthermore, the second term in the mass condition (29) is smaller than 10^{-7} for any position x^* of the discontinuity when $M > \beta = 20$. This means that assuming the truncated semi-support width $w_\rho \geqslant 20\rho$ leads to errors that are at least equal to 10^{-7}. Analogously, the Fourier transform of the bell function displayed in Figures 2a and 2b, for $\rho/W = 2/10$ and $\rho/W = 5/10$, respectively, has a non-compact support.

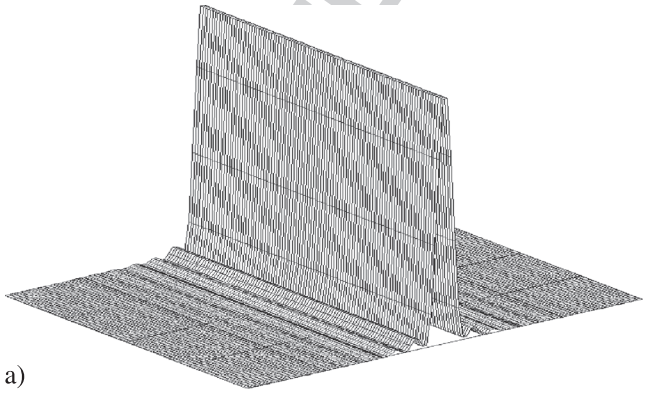

a)

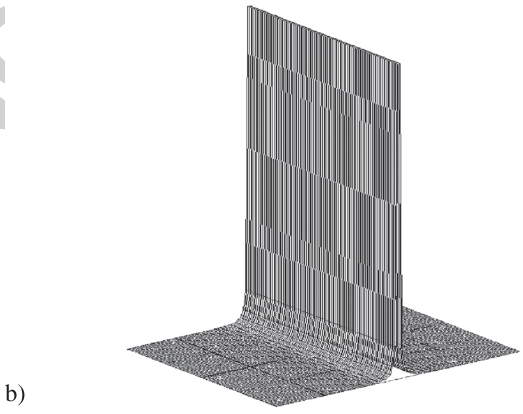

b)

Figure 1. Fourier transform $\hat{\varphi}_\rho^H$ of $\varphi_\rho^H = \max\{0, (1 - |t/\rho|)\}$ for $\rho/W = 2/10$ (a) and $\rho/W = 5/10$ (b), W being the width of the 2D domain considered.

DOI: 10.1002/nme

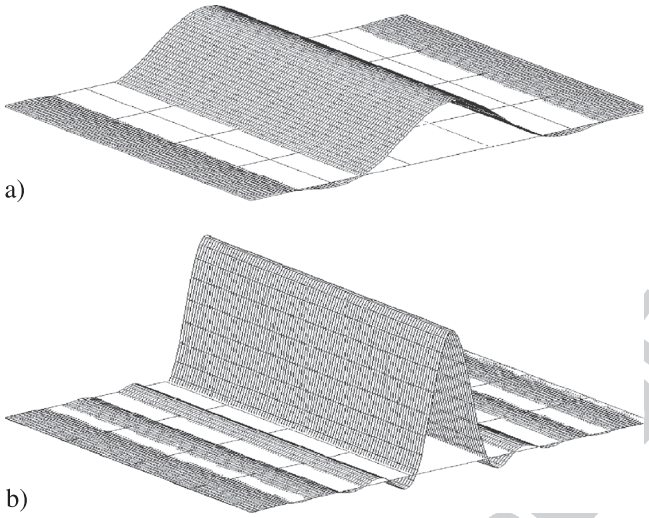

Figure 2. Fourier transform $\hat{\varphi}_\rho^B$ of $\varphi_\rho^B = (\max(0, (1 - |t/\rho|^2)))$ for $\rho/L = 2/10$ (a) and $\rho/W = 5/10$ (b), W being the width of the 2D domain considered.

Let us consider the Fourier transform of non-compact support regularized delta functions. For instance, the Gauss function (7) is identical to its Fourier transform

$$\hat{\varphi}^G = e^{-\pi\kappa^2}, \tag{30}$$

which is displayed in Figures 3a and 3b for $\rho/W = 0.2$ and $\rho/W = 0.5$, respectively, over a square domain of length $W = 10$ mm. Because $\int_{-\infty}^{+\infty} e^{-\pi t^2/\rho^2}\, dt = \rho$, and, thus, $\ell_\rho = \rho$ and $L = 1$, we can state that

$$\hat{\varphi}_\rho^G(0) = L = 1 \quad \left.\frac{\partial\hat{\varphi}^G}{\partial\kappa}\right|_{\kappa=0} = 0, \quad \left.\frac{\partial^2\hat{\varphi}^G}{\partial\kappa^2}\right|_{\kappa=0} \neq 0. \tag{31}$$

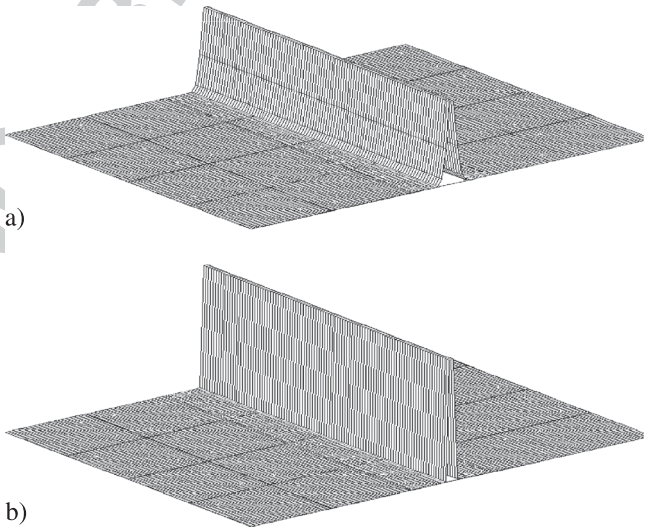

Figure 3. Fourier transform $\hat{\varphi}_\rho^G$ of $\varphi_\rho^G = \rho\sqrt{(\pi)}e^{-\pi^2\rho^2 s^2}$ for $\rho/W = 2/10$ (a) and $\rho/W = 5/10$ (b), W being the width of the 2D domain considered.

DOI: 10.1002/nme

Let us consider another non-compact support regularized delta function, namely the Laplacian regularized delta function (6). In this case, $\ell_\rho = 2\rho$, and thus, $L = 2$. The Fourier transform is

$$\hat{\varphi}_\rho^L = \frac{2\rho}{1 + 4\pi^2\rho^2\kappa^2} \tag{32}$$

F4 and it is shown in Figures 4a and 4b for $\rho/W = 0.2$ and $\rho/W = 0.5$, respectively, over a square domain of length $W = 10$ mm. We can recognize that

$$\hat{\varphi}_\rho^L(0) = 2 = L \qquad \left.\frac{\partial\hat{\varphi}_\rho^L}{\partial\kappa}\right|_{\kappa=0} = 0, \quad \left.\frac{\partial^2\hat{\varphi}_\rho^L}{\partial\kappa^2}\right|_{\kappa=0} \neq 0. \tag{33}$$

The mass condition for this case can be written as

$$M_0\left(\delta_\rho^L, p\,h, h\right) = 1 + \frac{1}{L}\sum_{\kappa\in\mathbb{Z},\kappa\neq 0} e^{-2\pi\,i\,\kappa\,p}\,\frac{2\,\rho}{1 + 4\,\pi^2\rho^2\,M^2\,\kappa^2}. \tag{34}$$

Note that the support of $\hat{\varphi}_\rho^L$ is not compact but that it has a monotonic decreasing behavior for increasing κ. Hence, the support width can be truncated. The second term in the mass condition (29) is smaller than 0.0001 for any dilation x^* when $M > \beta = 20$. This means that assuming the semi-support width $w_\rho \geqslant 20\rho$ leads to errors that are at least of the order 10^{-4}. Finally, $\hat{\varphi}_\rho^L$ and $\hat{\varphi}_\rho^G$ satisfy the moment conditions up to order 2.

A collection of the most relevant Fourier transforms is reported in Table II.

4.4. The dependence of the Fourier transform on ρ

F5 In the numerical analysis, the Laplacian function (6) is exploited. In Figure 5, it is shown that the support of the Fourier transform of the Laplacian function (6) increases for decreasing values of the regularization length ρ. Since the narrower the support width of the Fourier transform the lower the error, we expect that the error decreases for increasing values of ρ.

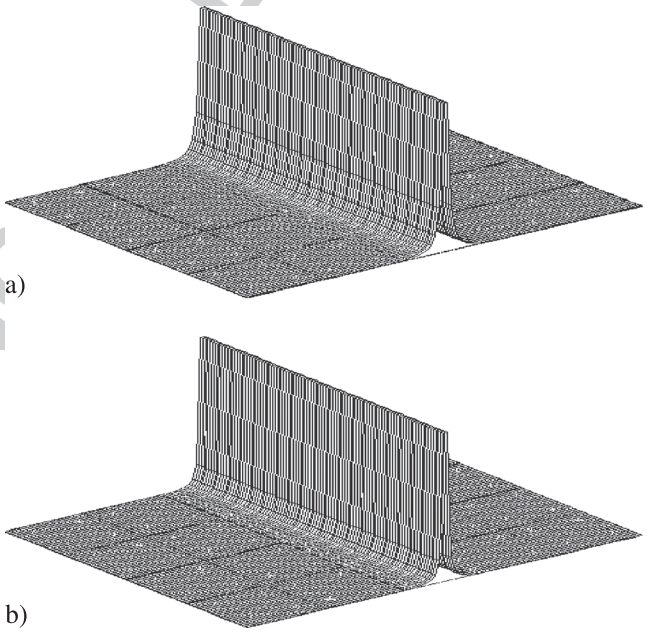

a)

b)

Figure 4. Fourier transform $\hat{\varphi}_\rho^L$ of $\varphi_\rho^L = 2\rho/(1 + 4\pi^2\rho^2\,\kappa^2)$ for $\rho/W = 2/10$ (a) and $\rho/W = 5/10$ (b), W being the width of the 2D domain considered.

DOI: 10.1002/nme

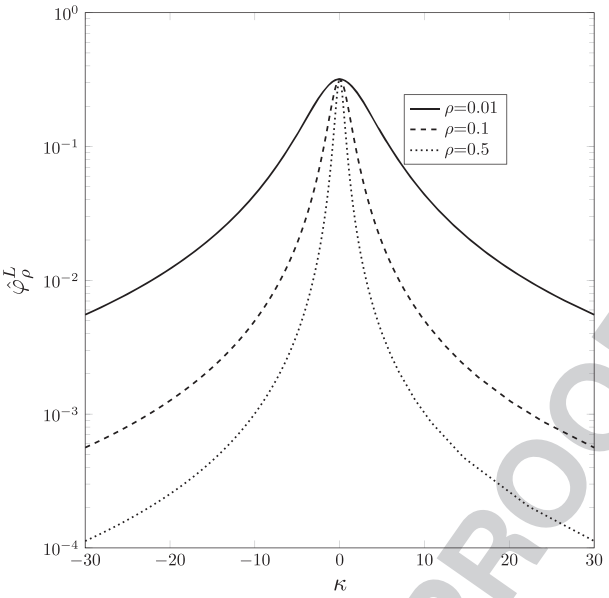

Figure 5. Fourier transform $\hat{\varphi}_\rho^L$ in the semi-logarithmic scale for variable ρ.

The comparison of Figure 3 with Figure 4 suggests that the truncated support width of the transform of the Gauss function is narrower than the truncated support width of the Fourier transform of the Laplacian function (6). This makes the Gauss function more advantageous to be used to regularize the singular delta function. However, the use of the Gauss function has the disadvantage that its antiderivative cannot be expressed as an elementary function. Thus, we cannot find compatible displacement and strain fields. On the contrary, although the Laplacian function (6) has non-compact support, its antiderivative is an elementary function. Thus, a displacement field can be constructed by means of its antiderivative, and a fully compatible displacement-strain relationship can be established.

4.5. Truncation error

The support of the Fourier transform can be truncated at a certain truncation length w_ρ from the regularized discontinuity. The truncation length depends on the error which we expect. For instance, Figure 5 shows that, at $|\kappa| = 20$, the order of the truncation error will be around 10^{-4} with $\rho = 0.5$ mm. If we want to decrease w_ρ, the price to pay is a larger truncation error. We next discuss this issue.

As regularized delta functions have the disadvantage that non vanishing errors for decreasing mesh size occur [21], we consider regularized delta functions with non-compact support, whose Fourier transform satisfies differentiability conditions. Then the support is truncated at a distance w_ρ such that $\varphi_\rho(w_\rho) < C$ where C is a certain tolerance. Truncation will introduce a further source of approximation which influences the analytical error. Let the truncation error be evaluated. Denote the truncated regularized delta function $\delta_\rho^{w_\rho}$ as

$$\delta_\rho^{w_\rho}(t) = \begin{cases} \delta_\rho(t) & \text{for } t \in [-w_\rho, w_\rho], \\ 0 & \text{otherwise}, \end{cases} \tag{35}$$

where w_ρ represents half the width of the truncated support of the regularized delta function. According to [17], the analytical error $\mathcal{E}_{w_\rho}$ associated with truncation can be neglected, provided that the mass condition and the first moment conditions hold

$$\int_{-w_\rho}^{w_\rho} \delta_\rho^{w_\rho}(t)\, dt = 1, \tag{36a}$$

DOI: 10.1002/nme

$$\int_{-w_\rho}^{w_\rho} \delta_\rho^{w_\rho}(t)\, t\, dt = 0. \tag{36b}$$

The first order moment condition (36b) is automatically satisfied because δ_ρ is an even function [39]. The error in the mass condition (36a) is the truncation error that depends on ρ and w_ρ. For instance, the assumption of the Laplacian regularized delta function (6) leads to an error in the mass condition equal to $2\,\rho\, e^{-\frac{w_\rho}{\rho}}$ that decreases for increasing w_ρ.

In the following we will use δ_ρ to indicate the truncated regularized delta function.

5. REGULARIZED SINGULARITIES IN THE XFEM FRAMEWORK

In this section, we define the kinematics (Section 5.1) and the variational formulation (Section 5.2) of the regularized XFEM framework adopted. The limit case for vanishing regularization length is discussed in Section 5.3.

5.1. Kinematics

The displacement field is approximated by enriching the space of the shape functions with additional enrichment functions added by the partition of unity method, that is, adding a term given by the product of the Heaviside function by the standard shape functions. Consider a body V with boundary ∂V. Let $\mathbf{u}$ be the displacement field. Displacements are imposed on the boundary ∂V_u, while tractions $\mathbf{f}$ on the portion ∂V_f, where ∂V_u and ∂V_f are disjoint. A displacement jump $[\mathbf{u}]_S = \mathbf{u}^+ - \mathbf{u}^-$ is considered across the surface S, with $S \cap V_u = \emptyset$ and $S \cap V_f = \emptyset$. Let $d(\mathbf{x})$ be the signed distance function of $\mathbf{x}$ from the surface S. We Heaviside function $\mathcal{H}(d(\mathbf{x}))$ such that $\mathcal{H}(d(\mathbf{x})) = 1$ for $d(\mathbf{x}) > 0$ and $\mathcal{H}(d(\mathbf{x})) = -1$ for $d(\mathbf{x}) \leq 0$. Volume V is subdivided into $\mathcal{N}_e$ finite elements connected at $\mathcal{N}$ nodes. The partition of unity approximation of the displacement field is

$$\mathbf{u}(\mathbf{x}) = \sum_{I \in \mathcal{N}} N_I(\mathbf{x})\mathbf{v}_I + \sum_{j \in \mathcal{S}} \mathcal{H}(d(\mathbf{x}))N_J(\mathbf{x})\mathbf{a}_I. \tag{37}$$

In (37), $\mathbf{u}_I$ and $\mathbf{a}_I$ denote the I-th nodal degrees of freedom corresponding to the standard part of the displacement field $\mathbf{u}$ and to the displacement jump, respectively.

For the subsequent developments, it is useful to express Equation (37) in the vector form

$$\mathbf{u}(\mathbf{x}) = \mathbf{N}(\mathbf{x})\mathbf{v} + \mathcal{H}(\mathbf{x})\mathbf{N}(\mathbf{x})\mathbf{a}, \tag{38}$$

where vectors $\mathbf{v}$ and $\mathbf{a}$ collect the nodal degrees of freedom and $\mathcal{H}(d(\mathbf{x}))$. The strain field is computed via compatibility from (37) as

$$\boldsymbol{\varepsilon}(\mathbf{x}) = \mathbf{B}(\mathbf{x})\mathbf{V} + \mathcal{H}(d(\mathbf{x}))\mathbf{B}(\mathbf{x})\mathbf{A} + \delta(\mathbf{x})\,\bar{\mathbf{N}}(\mathbf{x})\mathbf{A}, \tag{39}$$

where $\mathbf{B}$ is the compatibility matrix, $\bar{\mathbf{N}}$ is such that

$$\mathbf{N}\mathbf{A} \otimes \mathbf{n} \approx \bar{\mathbf{N}}\mathbf{A}, \tag{40}$$

and $\delta(\mathbf{x})$ is defined through the generalized gradient $\nabla\mathcal{H}(\mathbf{x}) = \delta(\mathbf{x})\mathbf{n}(\mathbf{x})$. Following the methodology proposed in [25, 29], regularization is carried out. The Heaviside function $\mathcal{H}$ is replaced with a regularized Heaviside function $\mathcal{H}_\rho$

$$\mathcal{H}_\rho(\mathbf{x}) = \int_{-\infty}^{d(\mathbf{x})} \delta_\rho(t)\, dt, \qquad \lim_{\rho \to 0} \mathcal{H}_\rho(\mathbf{x}) = \mathcal{H}(\mathbf{x}), \tag{41}$$

DOI: 10.1002/nme

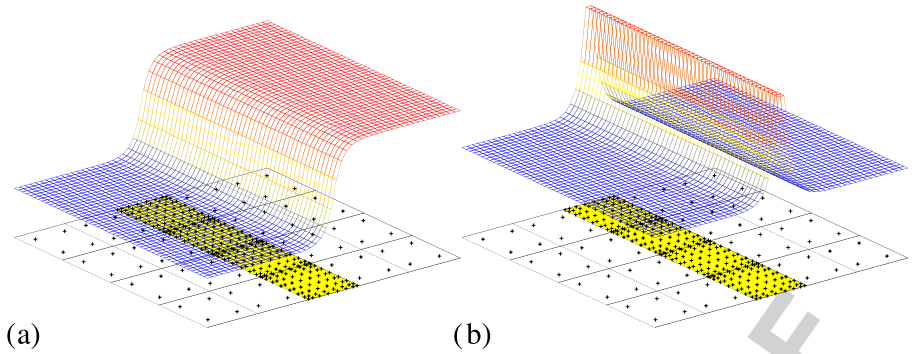

Figure 6. A qualitative sketch of regularized Heaviside (a) and Dirac delta function (b). Q3

and δ_ρ is defined by Equation (3). A qualitative picture of $\mathcal{H}_\rho$ and δ_ρ is proposed in Figure 6. F6

The regularized displacement writes

$$\mathbf{u}_\rho(\mathbf{x}) = \mathbf{N}(\mathbf{x})\mathbf{V} + \mathcal{H}_\rho(\mathbf{x})\mathbf{N}(\mathbf{x})\mathbf{A}, \tag{42}$$

whereas the strain field is

$$\boldsymbol{\varepsilon}_\rho(\mathbf{x}) = \mathbf{B}(\mathbf{x})\mathbf{V} + \mathcal{H}_\rho(\mathbf{x})\mathbf{B}(\mathbf{x})\mathbf{A} + \delta_\rho(\mathbf{x})\,\bar{\mathbf{N}}(\mathbf{x})\mathbf{A}. \tag{43}$$

The regularized strain (43) converges in a weak sense [36] to the singular strain (39).

5.2. *Variational formulation*

Let the material occupying volume V be elastic characterized by the constitutive matrix $\mathbf{E}$. The mechanical response of the regularized interface is governed by the constitutive matrix $K\bar{\mathbf{E}}$, where $K > 0$ is a scalar constitutive parameter that can be varied to reproduce soft and stiff interfaces, and $\bar{\mathbf{E}} = \mathbf{E}/t$ is the constitutive matrix of the bulk divided by the dimension t to get dimensionally consistent constitutive relationships. For instance, a soft interface is obtained with $K < 1$ and a stiff interface with $K \geqslant 1$. The dimensional consistency and the motivations for assuming $\bar{\mathbf{E}}$ in this way were thoroughly discussed in [25]. In particular, it was proven [25, 28] that a variational formulation based on the quadratic form of the regularized strain (43) leads to wrong results. A consistent variational formulations can be constructed treating the strain $\delta_\rho(\mathbf{x})\,\bar{\mathbf{N}}(\mathbf{x})\mathbf{A}$ as an equivalent eigenstrain [28]. In the following, the spatial dependence is omitted.

Let us set

$$\nabla\mathbf{U}_{\mathcal{H}_\rho} = \mathbf{B}\mathbf{V} + \mathcal{H}_\rho\mathbf{B}\mathbf{A}. \tag{44}$$

We introduce the energy

$$\mathcal{J} = \frac{1}{2}a\left(\nabla\mathbf{U}_{\mathcal{H}_\rho}, \nabla\mathbf{U}_{\mathcal{H}_\rho}\right) + \frac{1}{2}Kb(\mathbf{A},\mathbf{A}) - l(\mathbf{V}), \tag{45}$$

where

$$a\left(\nabla\mathbf{U}_{\mathcal{H}_\rho}, \nabla\mathbf{U}_{\mathcal{H}_\rho}\right) = \int_V \nabla\mathbf{U}_{\mathcal{H}_\rho} \cdot \mathbf{E}\,\nabla\mathbf{U}_{\mathcal{H}_\rho}\,dV, \tag{46a}$$

$$b(\mathbf{A},\mathbf{A}) = \int_V \delta_\rho\bar{\mathbf{N}}\mathbf{A} \cdot \bar{\mathbf{E}}\bar{\mathbf{N}}\mathbf{A}\,dV, \tag{46b}$$

$$l(\mathbf{V}) = \int_{\partial V_f} \mathbf{f} \cdot \mathbf{N}\mathbf{V}\,dV. \tag{46c}$$

DOI: 10.1002/nme

As extensively shown in [27, 28], the constitutive laws associated with the above variational formulation are

$$\boldsymbol{\sigma} = \mathbf{E}\left(\mathbf{B}(\mathbf{x})\mathbf{V} + \mathcal{H}_\rho(\mathbf{x})\mathbf{B}(\mathbf{x})\mathbf{A}\right) \tag{47}$$

in V, with the constraint that

$$\boldsymbol{\sigma} = K\,\bar{\mathbf{E}}\bar{\mathbf{N}}(\mathbf{x})\mathbf{A} \tag{48}$$

in the portion V_ρ where the regularization is active, $\bar{\mathbf{N}}$ being defined in Equation (40).

The total energy (45) can be written in a more compact form as

$$\mathcal{J} = \frac{1}{2}\mathbf{U}\cdot\mathbf{K}_{\mathcal{H}_\rho}\mathbf{U}\,dV + \frac{1}{2}K\mathbf{A}\cdot\mathbf{K}_{\delta_\rho}\mathbf{A} - l(\mathbf{V}), \tag{49}$$

where the stiffness matrix

$$\mathbf{K}_{\mathcal{H}_\rho} = \begin{pmatrix} \mathbf{K}^{vv}_{\mathcal{H}_\rho} & \mathbf{K}^{va}_{\mathcal{H}_\rho} \\ \mathbf{K}^{av}_{\mathcal{H}_\rho} & \mathbf{K}^{aa}_{\mathcal{H}_\rho} \end{pmatrix} \tag{50}$$

collects the submatrices

$$\mathbf{K}^{vv}_{\mathcal{H}_\rho} = \int_V \mathbf{B}^t\mathbf{E}\mathbf{B}\,dV, \quad \mathbf{K}^{av}_{\mathcal{H}_\rho} = \int_V \mathcal{H}_\rho\mathbf{B}^t\mathbf{E}\mathbf{B}\,dV = \mathbf{K}^{va^t}_{\mathcal{H}_\rho}, \quad \mathbf{K}^{aa}_{\mathcal{H}_\rho} = \int_V \mathcal{H}^2_\rho\mathbf{B}^t\mathbf{E}\mathbf{B}\,dV, \tag{51a}$$

while

$$\mathbf{K}_{\delta_\rho} = \int_V \delta_\rho\bar{\mathbf{N}}^t\bar{\mathbf{E}}\bar{\mathbf{N}}\,dV. \tag{52}$$

Following [27], the solving equations are obtained solving problem $\inf_{\mathbf{V},\mathbf{A}}\mathcal{J}$ as the stationarity conditions of function $\mathcal{J}$.

The accuracy analysis based on the Fourier transform and presented in Section 4.2 is used to evaluate the influence of the matrix (52) containing the regularized delta function on the computed results.

5.3. The limit case

Let us consider the case where the penalty-like term $b(\mathbf{A},\mathbf{A})$ vanishes according to the following laws

$$b(\mathbf{A},\mathbf{A}) = 0 \rightarrow \begin{cases} \mathbf{A} = \mathbf{0} \quad \text{and} \quad K \rightarrow \infty, \\ \text{or} \quad \mathbf{A} \neq \mathbf{0} \quad \text{and} \quad K \rightarrow 0. \end{cases} \tag{53}$$

In this special case,

$$\lim_{\rho\rightarrow\mathbf{0}} \mathbf{K}_{\mathcal{H}_\rho} = \mathbf{K}, \tag{54}$$

where

$$\mathbf{K} = \begin{pmatrix} \mathbf{K}^{vv} & \mathbf{K}^{va} \\ \mathbf{K}^{av} & \mathbf{K}^{aa} \end{pmatrix} \tag{55}$$

DOI: 10.1002/nme

is the standard stiffness matrix of the XFEM formulation [15], having set

$$\mathbf{K}^{vv} = \mathbf{B}^t\mathbf{E}\mathbf{B}, \qquad \mathbf{K}^{av} = \mathcal{H}\mathbf{B}^t\mathbf{E}\mathbf{B} = \mathbf{K}^{va^t}, \qquad \mathbf{K}^{aa} = \mathcal{H}^2\mathbf{B}^t\mathbf{E}\mathbf{B}. \tag{56a}$$

In the subsequent Section 6, the limit case based on the adoption of parameters leading to the fulfillment of Equation (53) is also investigated. The aim is to evaluate the accuracy of the regularization procedure when stress singularities at the regularized interface vanish. The accuracy of the quadrature procedure will then be related to the discrepancy between the computed stress values and those predicted by the analytical solution.

6. NUMERICAL RESULTS

As a benchmark problem, the slender three-dimensional solid shown in Figure 7 has been considered. The solid has length 2 mm and square cross section with area $A = 0.4 \times 0.4$ mm^2. The solid is clamped at one end and subjected to a traction of intensity $\sigma_{xx} = 1$ MPa prescribed at the free end. The material is characterized by a Young modulus $E = 10,000$ MPa and vanishing Poisson ratio. An inclined joint at the center of the bar is placed. Meshes of hexahedra are considered consisting of at least 5×5 elements in the cross section. The meshes have been refined at the center. Some meshes are displayed in Figure 8. In particular, the mesh a) has the minimum size $h = 0.0276$ mm along the longitudinal axis and the mesh (b) has the minimum size $h = 0.0067$ mm. These mesh sizes correspond to 1.3% and 0.3% of the longitudinal length, respectively. The elements containing Gauss points where the regularized Heaviside function is larger than a certain tolerance are enriched. The tolerance is related to the width of the support of the regularization. The influence of this width on the accuracy of the results is discussed in the simulations shown below. When the standard Gaussian quadrature is used, enriched hexahedra with a quadrature grid of 8^3 Gauss points were adopted. Non-enriched hexahedra contain 2^3 Gauss points.

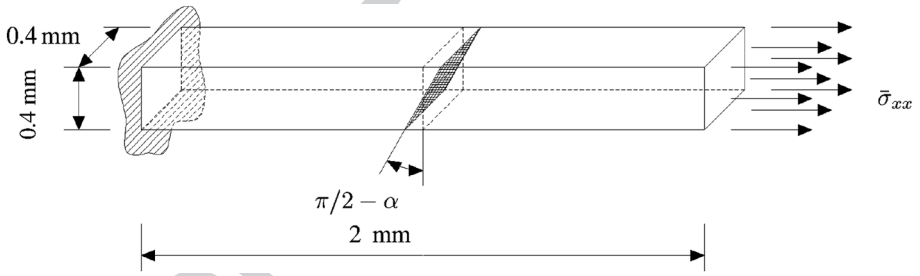

Figure 7. Geometry of the benchmark test; the solid is subjected to prescribed stress $\bar{\sigma}_{xx} = 1$ MPa.

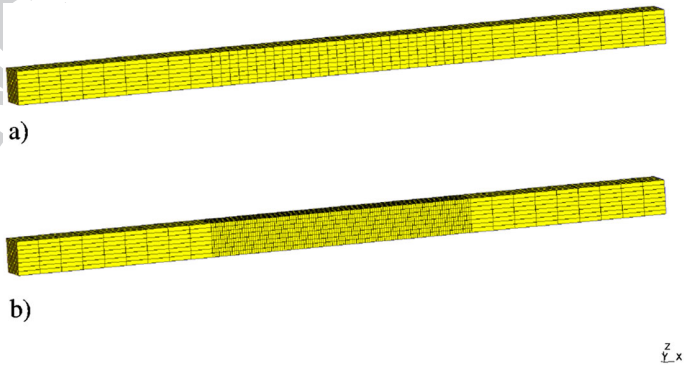

Figure 8. Typical meshes made of hexahedra adopted in the computation; the mesh a) has the minimum size $h = 0.0276$ mm along the longitudinal axis, the mesh b) has the minimum size $h = 0.0067$ mm along the longitudinal length = 2 mm.

DOI: 10.1002/nme

The accuracy obtained via Gaussian quadrature is compared with that obtained by means of CUBPACK adaptive quadrature FORTRAN tool. Mesh adaptive schemes [8] were excluded, to exploit the quadrature procedures already implemented in most commercial codes. We also consider meshes that are not aligned with the interface position, in line with the spirit of the XFEM [10, 37].

As an example of regularized delta function with non-compact and compact support, the Laplacian function (6) and the bell function (5) with $n = 2$, respectively, were adopted [34].

In Section 6.1, the issue of the stress singularities, which can arise in a tensile butt joint, is investigated. The accuracy in those cases where the stress singularity vanishes is studied in Section 6.2. The section ends with a critical discussion of the results in Section 6.3.

6.1. Stress singularities

F9 For a free edge bi-material joint such as that shown in Figure 9, a displacement singularity of strength $H\, r^{\lambda}$ and a stress singularity of strength $H\, r^{\lambda-1}$ may appear at the interface corner. In reference [40], the stress at the singularity was obtained as $\sigma = \bar{\sigma} w^{1-\lambda} a(\alpha_1, \alpha_2)$, where a is a function of the Dundurs parameters α_1 and α_2, $\bar{\sigma}$ is the remote stress, and w is the width of the bi-material strip.

Rao [41] determined the stress concentration in composites structures and bonded joints. For **F10** instance, let the interface be slanted by an inclination angle α (Figure 10a). When interfaces bond a soft material with a stiff material, like in the case in Figure 10a, Rao showed that for inclination angles $0 < \alpha < 118.7$, singular stress fields can arise at the interface. A similar but different case, shown in Figure 10b, is a soft joint with Young modulus E_3 and thickness h_3 between two materials with Young modulus E_1 and E_2 and thickness h_1 and h_2, respectively, where $E_1 h_1 > E_3 h_3$ and $E_2 h_2 > E_3 h_3$. The analytical solution predicts possible stress singularities at points A and C for $0^o < \alpha < 61.3^o$.

We next study two cases corresponding to vertical interface with $\alpha = \pi/2$ and inclined interface with $\alpha = \pi/3$. Whereas, in the former case, stress singularities are not expected, in the latter case they can occur according to [41].

With reference to the benchmark problem of Figure 7, we have first investigated the way the present model takes into account stress singularities. We next show that stress singularities are **F11** smoothed owing to the fact that the strain and stress fields are regularized. For instance, Figure 11 shows the decreasing trend of the stress singularity for increasing ρ when the typical mesh size is $h = 0.0067$ mm and $K = 0.0001$. In particular, the stress component σ_{xx} normalized with respect to the value $\bar{\sigma} = 1$ MPa corresponding to no singularities is plotted against the ρ values. The con- **F12** tour map of the maximum stress values displayed in Figure 12 shows that the stress singularities

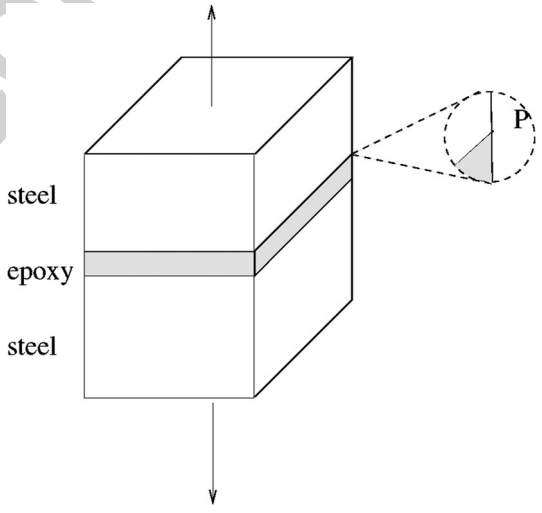

Figure 9. Adhesive butt joint under tension . A stress singularity is expected at point P [41, 42].

DOI: 10.1002/nme

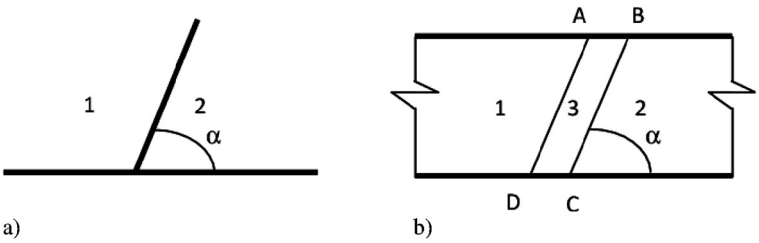

Figure 10. a) Interface between a soft material with E_1 and h_1, and a stiff material with E_2 and h_2: Singularities are possible for $0^\circ < \alpha < 118.7^\circ$ b) Adhesive soft joint between stiff materials; singularities are possible at A and C when $E_1 h_1,\ E_2 h_2 > E_3 h_3$ when $0^o < \alpha < 61.3^o$ according to [41].

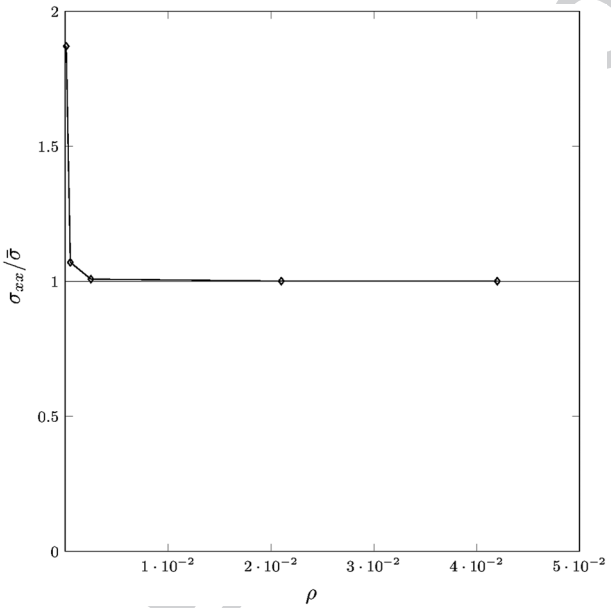

Figure 11. Slanted discontinuity with $\alpha = \pi/3$: $\sigma_{xx}/\bar{\sigma}$ for increasing ρ, where $\bar{\sigma} = 1$ MPa.

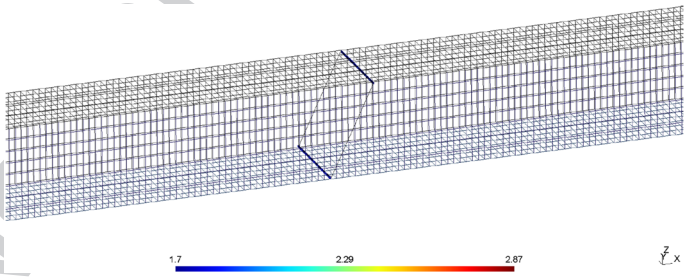

Figure 12. Slanted discontinuity with $\alpha = \pi/3$: Contours of the maximum stress values σ_{xx} for the mesh with $h = 0.0067$ mm, $K = 0.0001$, setting $\rho = 0.0001$ mm, and using the Laplacian regularized delta function and Gaussian quadrature.

Color Online, B&W in Print

are located where indicated by the theoretical results [41]. The results shown in Figures 11–12 were obtained by means of a Gaussian quadrature procedure by considering a regularization semi-support width equal to 30ρ. As motivated in Section 6.2 and discussed in Section 6.3, this width makes the truncation error negligible. Figure 13 shows the enriched elements in green at the center of the bar. Moreover, the stress peak value converges when the mesh size h is refined. In particular, Figure 14 shows the contour plot of the stress component $\sigma_x x$ obtained with $h = 0.0033$ mm and setting $\rho = 0.0001$ mm, which corresponds to a ratio $\rho/h = 0.03$.

F13
F14

DOI: 10.1002/nme

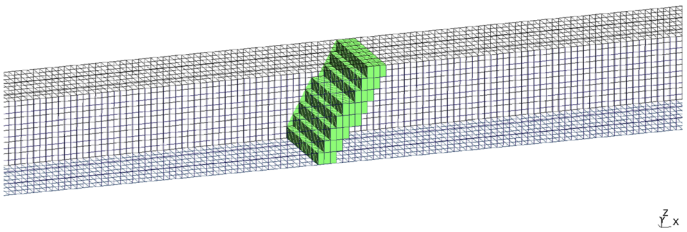

Figure 13. Slanted discontinuity with $\alpha = \pi/3$: adopted enriched elements for the mesh having $h = 0.0067$ mm, setting $K = 0.0001$, $\rho = 0.0001$ mm; the Laplacian regularized delta function and Gaussian quadrature were employed.

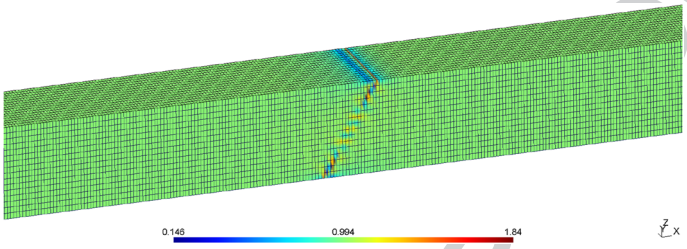

Figure 14. Slanted discontinuity with $\alpha = \pi/3$: Stress profile for the finest mesh having $h = 0.0033$ mm, setting $K = 0.0001$, $\rho = 0.0001$ mm; the Laplacian weight function and Gaussian quadrature were employed.

Furthermore, Figure 11 shows that for $\rho \geqslant 0.021$ mm the stress singularities are smoothed, and the stress field converges to the solution $\sigma_{xx} = \bar{\sigma}_{xx}$ everywhere. Although the regularized XFEM is perfectly able to reproduce stress concentrations by using very small values of ρ, in Section 6.2, the value $\rho = 0.021$ mm is adopted when a soft joint is modeled so that the stress singularity is ruled out.

6.2. *Accuracy evaluation*

To evaluate the accuracy of a quadrature procedure based on standard Gaussian quadrature, a comparison with the analytical solution is required. Because the tensile butt joint problem was shown to be characterized by the occurrence of stress singularities [41–43], we separate the effect of the choice of the quadrature procedure from the effect of the stress singularity, and we discuss here those cases where the singularity is ruled out. This is obtained considering either a stiff joint with very large stiffness, in particular $K = 10,000$, or a value of the regularization parameter $\rho = 0.021$ mm, owing to the conclusions drawn in Section 6.1. Note that the proposed approach is general, as it can be employed for both narrow and large regularization length with respect to the mesh size.

We study the convergence properties of regularized delta functions with non-compact and compact support in two ways: by mesh refinement for fixed support width and by varying the support width for a fixed mesh.

The norm

$$\mathcal{E}_\infty = \sup\left\{\left|\sigma^h_{xx} - \bar{\sigma}_{xx}\right|\right\} \tag{57}$$

has been used for evaluating the accuracy of the results in the cases where the stress singularity vanishes, so that the analytical solution predicts that the xx components of the computed stress, σ^h_{xx} should converge to the prescribed value $\bar{\sigma}_{xx}$ everywhere in the domain. Moreover, we have also used the error related to the computed displacement of the free end $u^h(L)$

$$\mathcal{E}_u = \left|u^h(L) - \bar{u}\right| \tag{58}$$

DOI: 10.1002/nme

where $\bar{u}$ is the analytical value. First the case of the vertical discontinuity is considered. In Figure 15a, the convergence in the case of the Laplacian function (6) is shown for decreasing mesh size h. The error is indicated in the logarithmic scale. The "$\diamond$" continuous line indicates the error $\mathcal{E}_\infty$ (57) using the Gaussian procedure, whereas the "$\square$" continuous line interpolates the error obtained by the Adaptive procedure. The same markers with the dashed line indicate the homologous errors obtained by adopting the displacement norm $\mathcal{E}_u$ (58). The parameter K has been set equal to 10,000, whereas the regularization parameter $\rho = 0.021$ mm and truncated semi-support $w_\rho = 10\rho$ have been taken. The error evaluated according to $\mathcal{E}_\infty$ (57) is usually larger than that evaluated according to the norm (58). Hence, in the results shown hereafter, the error $\mathcal{E}_\infty$ is adopted. In Figure 15b, the

F15

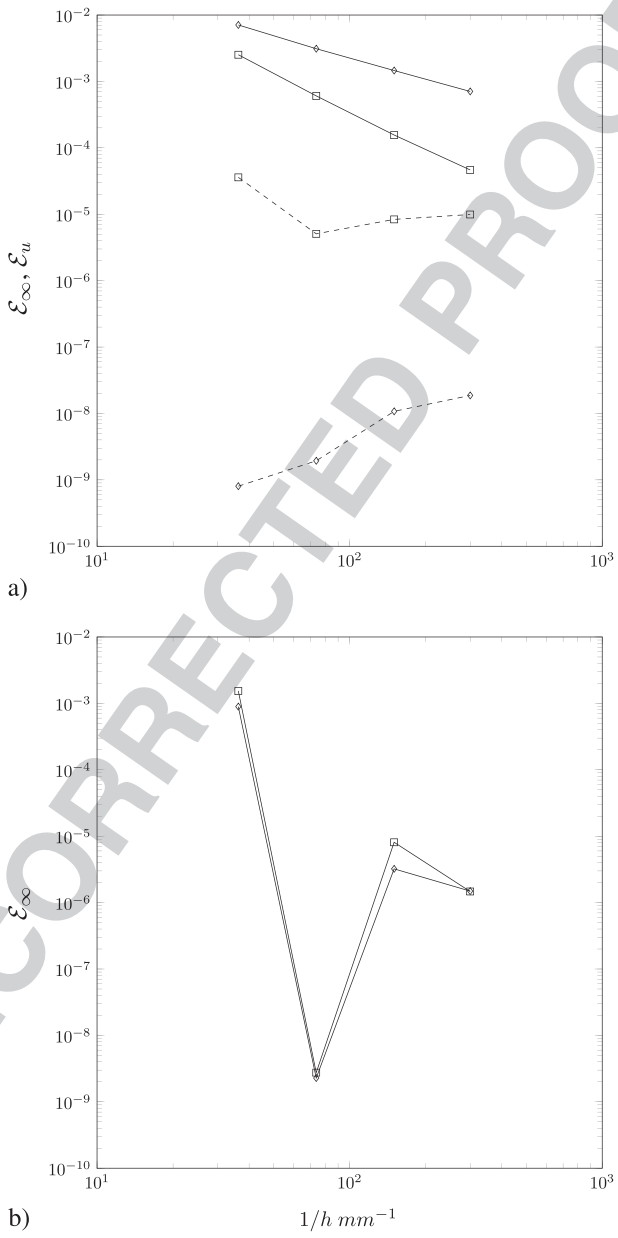

Figure 15. We display the case of vertical discontinuity with $\alpha = \pi/2, K = 0.0001, \rho = 0.021$ mm, truncation length $w_\rho = 10\rho$, non-compact support Laplacian function (a), and compact support bell function (b). The "$\diamond-$" and "$\diamond--$" lines correspond to the error $\mathcal{E}_\infty$ (57) computed with the Gaussian quadrature and the adaptive quadrature, respectively; the "$\square-$" and "$\square--$" lines correspond to the error $\mathcal{E}_u$ (58) obtained with the Gaussian and the adaptive quadrature procedure, respectively.

DOI: 10.1002/nme

accuracy obtained by using the bell function is shown. Convergence is assessed with respect to the error $\mathcal{E}_\infty$ (57) for $K = 0.0001$, and semi-support width $w_\rho = 10\,\rho = 0.21$ mm corresponding to the 10% of the length of the structural member. The □ and ◇ markers denote the Gaussian and the adaptive quadrature, respectively.

The slanted discontinuity case with $\alpha = \pi/3$ has been taken into consideration. In order to establish a comparison with the results shown for the vertical discontinuity case, the same parameters $K = 0.0001$, and $\rho = 0.021$ mm have been chosen. In Figure 16a and 16b, the convergence of the error $\mathcal{E}_\infty$ (57) for increasing h is shown for the Laplacian regularized delta function, and the bell function, respectively. The □ and ◇ markers denote Gaussian and adaptive quadrature, respectively. It can be noted that the trend of $\mathcal{E}_\infty$ (57) is oscillating when the bell function is used. As a general

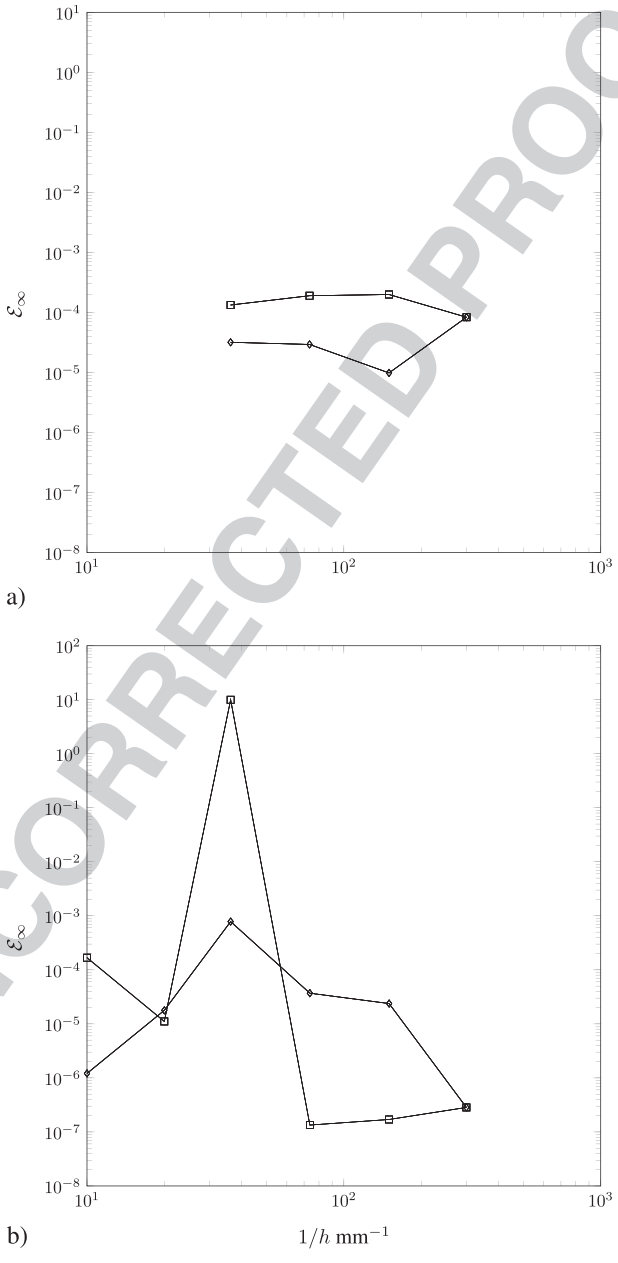

Figure 16. Slanted discontinuity with $\alpha = \pi/3$, and non-compact support (Laplacian) function (a), compact support (bell) function (b): Convergence of the error $\mathcal{E}_\infty$ (57) for $K = 0.0001, \rho = 0.021$ mm. □ and ◇ markers indicate Gaussian and adaptive quadrature, respectively.

DOI: 10.1002/nme

trend, it was indeed observed that the error can vary in a wide range independently of the mesh size. This implies that the adaptive quadrature procedure loses convergence even for very fine meshes. Therefore, it can be drawn that the use of the bell function is not reliable when the discontinuity is slanted.

It is worth noting that the proposed regularized approach is fully effective also for values of the regularization parameter that are very small with respect to the mesh size. Figure 17 shows indeed **F17** the convergence of the error $\mathcal{E}_\infty$ (57) for $\rho = 0.0002$ mm, which is 0.02% of the length of the structural member, and corresponds to $\rho/h = 0.06$ when the finest mesh with $h = 0.0033$ mm is chosen. The semi-support width $w_\rho = 10\rho = 0.002$ mm, corresponding to 0.2 % of the length of the structural member.

Figures 18 display the accuracy of the approximation for increasing width of the support of **F18** the Laplacian function (6). The parameter K was set equal to 0.0001 in Figure 18a and equal to 10,000 in Figure 18b. The "$\diamond$" markers denote the results obtained by adopting a truncated support of 20ρ. The "$\times$" and "$\square$" markers are associated with the errors obtained by truncating the support at a length equal to 40ρ and 60ρ, respectively. In Figure 18b, the perfect interface is reproduced and the jump discontinuity vanishes. Hence, the accuracy is independent of the width of the truncated support.

The influence of the truncation error on the error $\mathcal{E}_\infty$ (58) obtained with Gaussian quadrature in the case of slanted discontinuity with $\alpha = \pi/3$ is highlighted further in Figures 19. The figures **F19** refer to the mesh with minimum mesh size $h = 0.0067$ mm. In particular, in Figure 19a, the contour plot of the error on the stress component $\boldsymbol{\sigma}_{xx}$ is shown for the case of $\rho = 0.021$ mm and a semi-support width equal to $10\rho = 0.21$mm, whereas $K = 0.0001$. This set of parameters refer to the case of a soft joint. In Figures 19b and 19c, the semi-support widths equal to $20\rho = 0.42$ mm and $30\rho = 0.63$ mm, respectively, were adopted. Figure 19d shows the error $\mathcal{E}_\infty$ (57) obtained in the perfect (stiff) interface case by assuming $K = 10,000$. It has been obtained for fixed value of $\rho = 0.021$ mm and semi-support width equal to 20ρ. For the stiff interface case, the contour plot of the error corresponding to the semi-support width 30ρ is similar to that shown in Figure 19d.

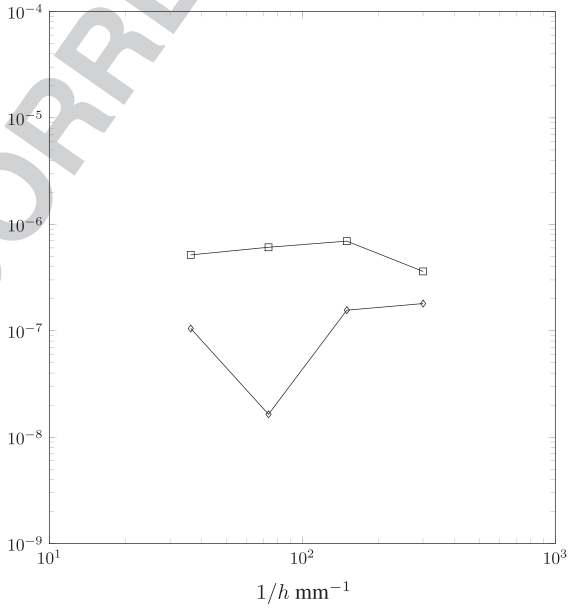

Figure 17. Slanted discontinuity with $\alpha = \pi/3$ and non-compact support (Laplacian) function: Convergence of the error $\mathcal{E}_\infty$ (57) for $K = 10,000$, $\rho = 0.0002$ mm. $\square$ and $\diamond$ markers indicate Gaussian and adaptive quadrature, respectively.

DOI: 10.1002/nme

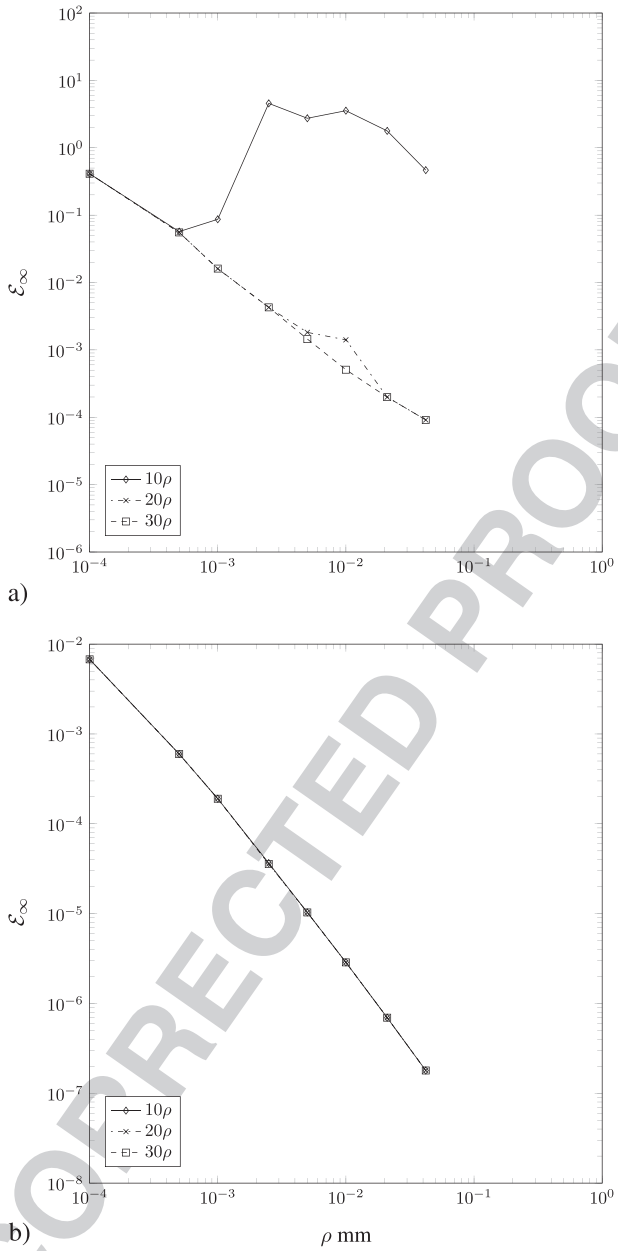

Figure 18. Slanted discontinuity with $\alpha = \pi/3$ and non-compact support (Laplacian): Convergence of the error $\mathcal{E}_\infty$ (57) for increasing width of the support with $K = 0.0001$ (a) and $K = 10,000$ (b). The markers "$\diamond$," "$\times$," and "$\square$" indicate truncation length $w_\rho = 10\rho$, $w_\rho = 20\rho$, and $w_\rho = 30\rho$, respectively.

6.3. Discussion of the results

In Section 4.2, it has been shown that the error implied by the replacement of the singular delta function with the regularized delta function within the stiffness matrix is related to the values that the Fourier transform of the regularized delta function reaches at increasing distances from the discontinuity. If the Fourier transform of a regularized delta function has an oscillatory character, this oscillatory character makes the truncation not possible. Conversely, if the Fourier transform has a compact support or a support that can be truncated, then the moment conditions can be satisfied for certain values of ρ. In particular, the Laplacian regularized delta function has a Fourier Transform of the latter type, whereas the bell function has a Fourier transform of the former type.

DOI: 10.1002/nme

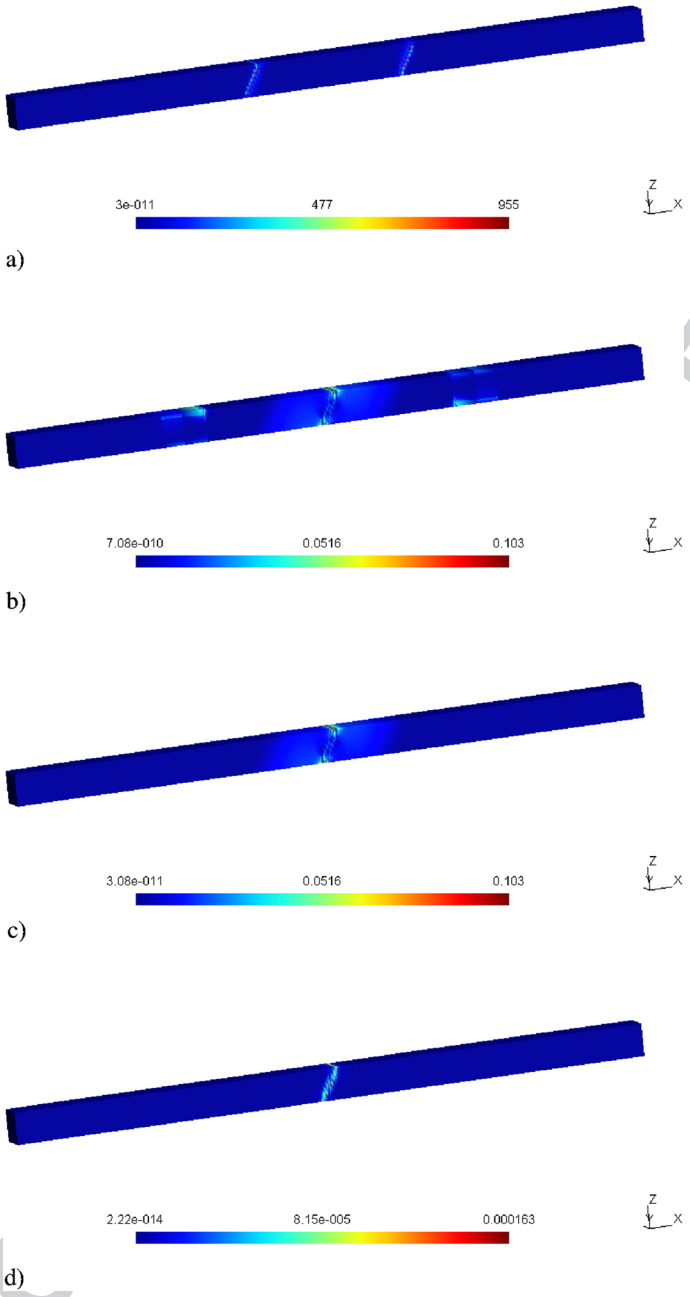

Figure 19. Slanted discontinuity with $\alpha = \pi/3$: The figures display the error $\mathcal{E}_\infty$ (57) in % on the stress component $\boldsymbol{\sigma}_{xx}$ obtained with the Gaussian quadrature procedure, being the exact value for vanishing singularity $\boldsymbol{\sigma}_{xx} = 1$ MPa. The minimum mesh size is $h = 0.0067$ mm, and $\rho = 0.021$ mm. In a), b), and c) $K = 0.0001$, and the truncation length w_ρ is $10\rho, 20\rho$ and 30ρ, respectively. In d), $K = 10,000$, and $w_\rho = 20\rho$.

The simulations in Section 6 have confirmed that the errors do not decrease for decreasing mesh size when the bell-type regularized delta function is used: The errors oscillate and there is no warranty that the procedure converges. The adaptive quadrature algorithm loses convergence for certain meshes. Therefore, a procedure based on the adoption of the bell function is not robust and effective. Conversely, when the Laplacian function is used, the convergence has been shown to be slower but effective, and the simple integration procedure based on Gaussian quadrature is sufficient to acquire consistent and reliable results. As expected according to the similarity rule of the Fourier transforms,

DOI: 10.1002/nme

the convergence rate increases when the truncated support width increases, being acceptable for a truncated semi-support width in the range 20ρ–30ρ.

Moreover, from Figure 19, it can be drawn that the truncation error vanishes when the truncated support width increases. When the Gaussian quadrature procedure is applied, the error decreases for increasing mesh size, whereas when adaptive quadrature is exploited, the error is smaller even for coarse meshes.

7. CONCLUSIONS

Regularized delta functions with compact support are easy to be implemented. However, quadrature procedures based on regularized delta functions with compact support are not robust and stable, because Gaussian and adaptive quadrature fail to find a solution for any position of the regularized displacement discontinuity.

In this paper, we have shown that the Fourier transform of the regularized delta function simplifies the choice of the proper regularized delta function. Indeed, regularized delta functions with Fourier transforms displaying narrow support lead to the lowest error. In particular, the error that affects the computations exhibits an oscillating trend for decreasing mesh size in the case of regularized delta functions with compact support and a stable and monotonically decreasing trend in the case of regularized delta functions with non-compact support. As for regularized delta functions with non-compact support, the truncation error of the Fourier transforms affects the total error. The order of the truncation error depends on the support width of the Fourier transform and decreases for increasing regularization length.

The examples shown in this paper prove that a regularization procedure based on the Laplacian function is robust and effective and that Gaussian quadrature leads to an acceptable compromise between simplicity and accuracy, provided that the mesh is sufficiently fine with respect to the regularization support.

ACKNOWLEDGEMENTS

E.B. and A.T. acknowledge the support of the Italian PRIN Fund 2009XWLFKW *Multi-scale modelling of materials and structures*.

REFERENCES

1. Chorin A. Numerical study of slightly viscous flow. *Journal of Fluid Mechanics* 1973; **57**:785–796.
2. Peskin C. Numerical analysis of blood flow in the heart. *Journal of Computational Physics* 1977; **25**:220–252.
3. Beyer R, Leveque R. Analysis of a one-dimensional model for the immersed boundary method. *SIAM Journal of Numerical Analysis* 1992; **29**:332–364.
4. Chen LQ. Phase field models for microstructure evolution. *Annual Review of Materials Research* 2002; **32**:113–140.
5. Lee H, Kim J. Regularized Dirac delta functions for phase field models. *International Journal for Numerical Methods in Engineering* 2012; **91**:269–288.
6. Leveque R, Li Z. The immersed interface method for elliptic equations with discontinuous coefficients and singular sources. *SIAM Journal of Numerical Analysis* 1994; **31**:1019–1044.
7. Abbas S, Alizada A, Fries T. The XFEM for high-gradient solutions in convection-dominated problems. *International Journal for Numerical Methods in Engineering* 2010; **82**:1044–1072.
8. Mousavi S, Pask J, Sukumar N. Efficient adaptive integration of functions with sharp gradients and cusps in n-dimensional parallelepipeds. *International Journal for Numerical Methods in Engineering* 2012; **91**:343–357.
9. Xu J, Lee C, Tan K. A two-dimensional co-rotational Timoshenko beam element with XFEM formulation. *Computational Mechanics* 2012; **49**:667–683.
10. Moës N, Dolbow J, Belytschko T. A finite element method for crack growth without remeshing. *International Journal for Numerical Methods in Engineering* 1999; **46**:131–150.
11. Löhnert S, Müller-Hoeppe D, Wriggers P. 3D corrected XFEM approach and extension to finite deformation theory. *International Journal for Numerical Methods in Engineering* 2011; **86**:431–452.
12. Müller B, Kummer F, Oberlack M, Wang Y. Simple multidimensional integration of discontinuous functions with application to level set methods. *International Journal for Numerical Methods in Engineering* 2012; **92**:637–651.
13. van Dooren P, de Ridder L. An adaptive algorithm for numerical integration over an n-dimensional cube. *Journal of Computational and Applied Mathematics* 1976; **2**:207–217.

DOI: 10.1002/nme

14. Mousavi S, Sukumar N. Generalized Gaussian quadrature rules for discontinuities and crack singularities in the extended finite element method. *Computer Methods in Applied Mechanics and Engineering* 2012; **199**:3237–3249.
15. Ventura G. On the elimination of quadrature subcells for discontinuous functions in the extended finite-element method. *International Journal for Numerical Methods in Engineering* 2006; **66**:761–795.
16. Tornberg A. Multi-dimensional quadrature of singular and discontinuous functions. *BIT Numerical Mathematics* 2002; **42**:644–669.
17. Tornberg A, Engquist B. Regularization techniques for numerical approximation of PDEs with singularities. *Journal of Scientific Computing* 2003; **19**:527–552.
18. Brandt A, Lubrecht AA. Multilevel matrix multiplication and fast solution of integral equations. *Journal of Computational Physics* 1990; **90**:348–370.
19. Benvenuti E, Tralli A. The fast Gauss transform for non-local integral FE models. *Communications in Numerical Methods in Engineering* 2006; **22**:505–533.
20. Osher S, Sethian J. Fronts propagating with curvature dependent speed: algorithms based on Hamilton-Jacobi formulations. *Journal of Computational Physics* 1988; **79**:12–49.
21. Zahedi S, Tornberg A. Delta function approximations in level set methods by distance function extension. *Journal of Computational Physics* 2010; **229**:2199–2219.
22. Belytschko T, Gracie R, Ventura G. A review of the extended/generalized finite element methods for material modelling. *Modelling and Simulation in Materials Science and Engineering* 2009; **17**. DOI: 10.1088/0965-0393/17/4/043001. Q4
23. Fries T, Belytschko T. The extended/generalized finite element method: an overview of the method and its applications. *International Journal for Numerical Methods in Engineering* 2010; **84**:253–304.
24. Gravouil A, Pierres E, Baietto M. Stabilized globallocal X-FEM for 3D non-planar frictional crack using relevant meshes. *International Journal for Numerical Methods in Engineering* 2011; **88**:1449–1475.
25. Benvenuti E, Tralli A, Ventura G. A regularized XFEM model for the transition from continuous to discontinuous displacements. *International Journal for Numerical Methods in Engineering* 2008; **74**:911–944.
26. Benvenuti E. Mesh-size-objective XFEM for regularized continuous discontinuous transition. *Finite Elements in Analysis and Design* 2011; **47**:1326–1336.
27. Benvenuti E, Ventura G, Ponara N, Tralli A. Variationally consistent extended FE model for 3D planar and curved imperfect interfaces. *Computer Methods in Applied Mechanics and Engineering* 2013; **267**:434–457.
28. Benvenuti E. XFEM with equivalent eigenstrain for matrix-inclusion interfaces. *Computational Mechanics* 2014; **53**:893–908.
29. Benvenuti E. A regularized XFEM framework for embedded cohesive interfaces. *Computer Methods in Applied Mechanics and Engineering* 2008; **197**:4367–4378.
30. Benvenuti E, Tralli A. Simulation of finite-width process zone for concrete-like materials. *Computational Mechanics* 2012; **50**:479–497.
31. Benvenuti E, Vitarelli O, Tralli A. Delamination of FRP-reinforced concrete by means of an extended finite element formulation. *Composite Part B: Engineering* 2012; **43**:3258–3269.
32. Ventura G, Gracie R, Belytschko T. Fast integration and weight function blending in the extended finite element method. *International Journal for Numerical Methods in Engineering* 2009; **77**:1–29.
33. Fries T. A corrected XFEM approximation without problems in blending elements. *International Journal for Numerical Methods in Engineering* 2007; **75**:503–532.
34. Patzák B, Jirásek M. Process zone resolution by extended finite elements. *Engineering Fracture Mechanics* 2003; **70**:957–977.
35. Iarve E, Gurvich M, Mollenhauer D, Rose C, Dávila C. Mesh-independent matrix cracking and delamination modeling in laminated composites. *International Journal for Numerical Methods in Engineering* 2011; **88**:749–773.
36. Kolmogorov A, Fomin S. *Introductory Real Analysis*. Dover, 1975.
37. Areias P, Belytschko T. Two-scale method for shear bands: thermal effects and variable bandwidth. *International Journal for Numerical Methods in Engineering* 2007; **72**:658–696.
38. Tornberg A, Engquist B. Numerical approximations of singular source terms in differential equations. *Journal of Computational Physics* 2004; **200**:462–488.
39. Benvenuti E, Ventura G, Ponara N. Finite element quadrature of regularized discontinuous and singular level set functions in 3D problems. *Algorithms* 2012; **5**:529–544.
40. Akisanya A, Fleck N. Interfacial cracking from the free-edge of a long bi-material strip. *International Journal of Solids and Structures* 1997; **34**:1645–1665.
41. Rao A. Stress concentrations and singularities at interface corners. *Zeitschrift fur Angewandte Mathematik und Mechanik* 1971; **51**:395–406.
42. Sinclair G. Stress singularities in classical elasticity–I: removal, interpretation, and analysis. *Applied Mechanics Reviews* 2004; **57**:251–297.
43. Sinclair G. Stress singularities in classical elasticity–II: asymptotic identification. *Applied Mechanics Reviews* 2004; **57**:385–439.

DOI: 10.1002/nme

Author Query Form

Journal: International Journal for Numerical Methods in Engineering

Article: nme_4788

Dear Author,

During the copyediting of your paper, the following queries arose. Please respond to these by annotating your proofs with the necessary changes/additions.

- If you intend to annotate your proof electronically, please refer to the E-annotation guidelines.
- If you intend to annotate your proof by means of hard-copy mark-up, please refer to the proof mark-up symbols guidelines. If manually writing corrections on your proof and returning it by fax, do not write too close to the edge of the paper. Please remember that illegible mark-ups may delay publication.

Whether you opt for hard-copy or electronic annotation of your proofs, we recommend that you provide additional clarification of answers to queries by entering your answers on the query sheet, in addition to the text mark-up.

Query No.	Query	Remark
Q1	AUTHOR: "We need to precise the..." This sentence has been reworded for clarity. Please check and confirm if it is correct.	see note
Q2	AUTHOR: "We Heaviside function..." The meaning of this sentence is not clear; please rewrite or confirm that the sentence is correct.	see note
Q3	AUTHOR: Figures 6, 12, 13, 14, and 19 are recommended for color online and in print. Please check.	color online
Q4	AUTHOR: Please provide page range for Reference 22.	there is no page

WILEY-BLACKWELL

USING e-ANNOTATION TOOLS FOR ELECTRONIC PROOF CORRECTION

Required software to e-Annotate PDFs: Adobe Acrobat Professional or Adobe Reader (version 7.0 or above). (Note that this document uses screenshots from Adobe Reader X)
The latest version of Acrobat Reader can be downloaded for free at: http://get.adobe.com/uk/reader/

Once you have Acrobat Reader open on your computer, click on the Comment tab at the right of the toolbar:

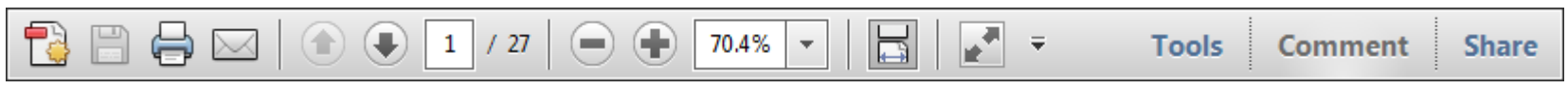

This will open up a panel down the right side of the document. The majority of tools you will use for annotating your proof will be in the Annotations section, pictured opposite. We've picked out some of these tools below:

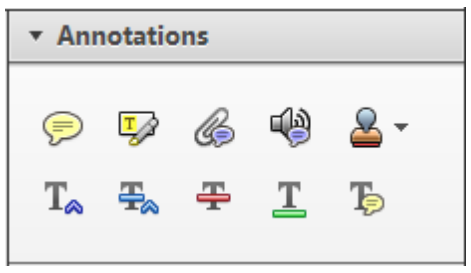

1. Replace (Ins) Tool – for replacing text.

Strikes a line through text and opens up a text box where replacement text can be entered.

How to use it

- Highlight a word or sentence.
- Click on the Replace (Ins) icon in the Annotations section.
- Type the replacement text into the blue box that appears.

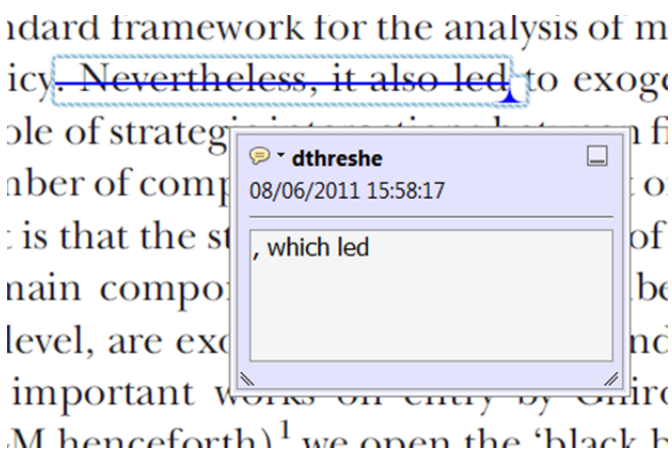

2. Strikethrough (Del) Tool – for deleting text.

Strikes a red line through text that is to be deleted.

How to use it

- Highlight a word or sentence.
- Click on the Strikethrough (Del) icon in the Annotations section.

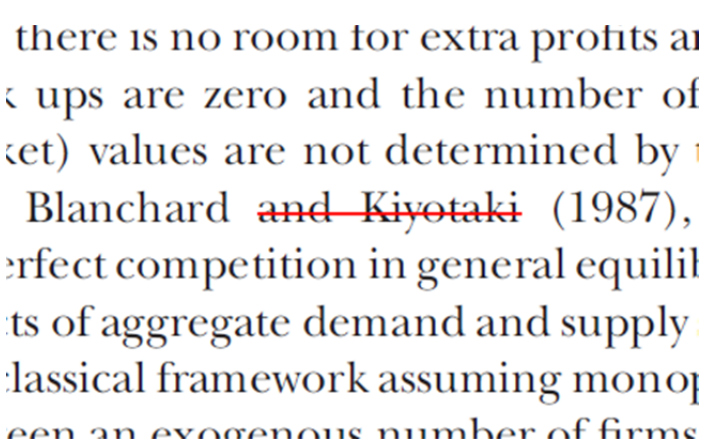

3. Add note to text Tool – for highlighting a section to be changed to bold or italic.

Highlights text in yellow and opens up a text box where comments can be entered.

How to use it

- Highlight the relevant section of text.
- Click on the Add note to text icon in the Annotations section.
- Type instruction on what should be changed regarding the text into the yellow box that appears.

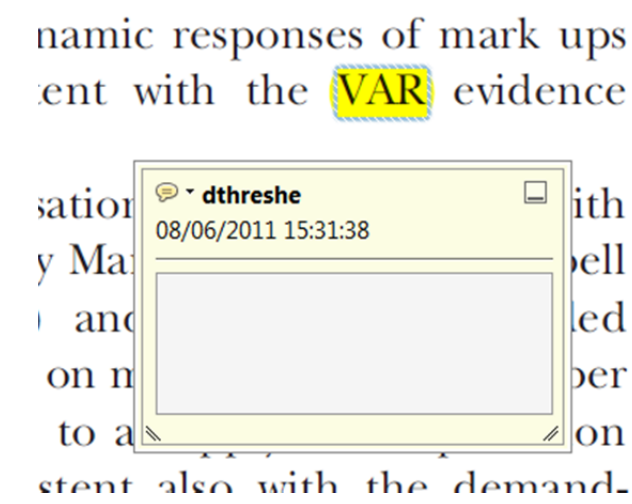

4. Add sticky note Tool – for making notes at specific points in the text.

Marks a point in the proof where a comment needs to be highlighted.

How to use it

- Click on the Add sticky note icon in the Annotations section.
- Click at the point in the proof where the comment should be inserted.
- Type the comment into the yellow box that appears.

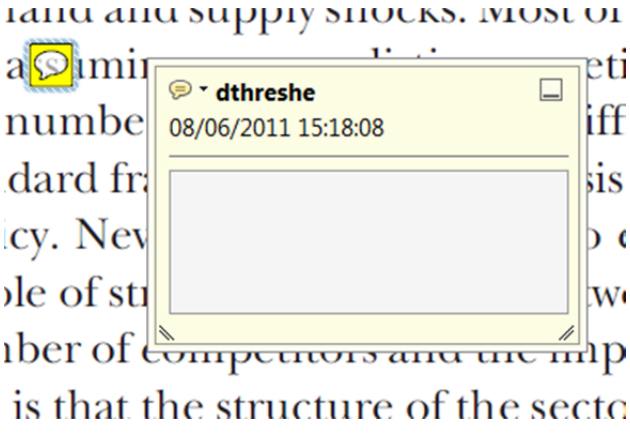

WILEY-BLACKWELL

USING e-ANNOTATION TOOLS FOR ELECTRONIC PROOF CORRECTION

5. Attach File Tool – for inserting large amounts of text or replacement figures.

Inserts an icon linking to the attached file in the appropriate pace in the text.

How to use it

- Click on the Attach File icon in the Annotations section.
- Click on the proof to where you'd like the attached file to be linked.
- Select the file to be attached from your computer or network.
- Select the colour and type of icon that will appear in the proof. Click OK.

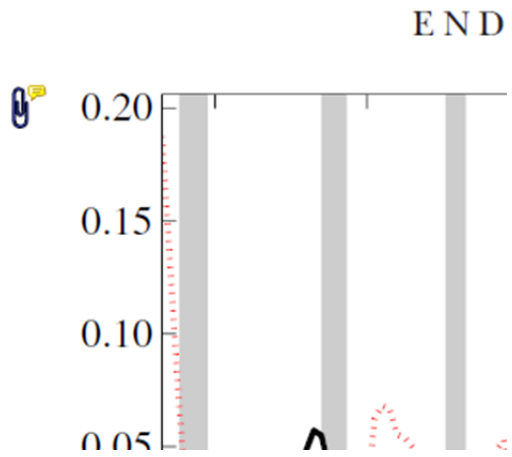

6. Add stamp Tool – for approving a proof if no corrections are required.

Inserts a selected stamp onto an appropriate place in the proof.

How to use it

- Click on the Add stamp icon in the Annotations section.
- Select the stamp you want to use. (The Approved stamp is usually available directly in the menu that appears).
- Click on the proof where you'd like the stamp to appear. (Where a proof is to be approved as it is, this would normally be on the first page).

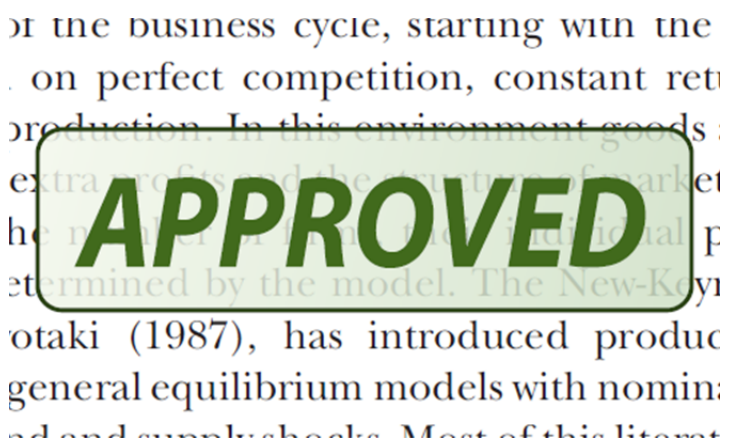

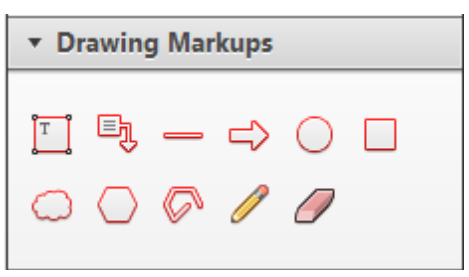

7. Drawing Markups Tools – for drawing shapes, lines and freeform annotations on proofs and commenting on these marks.

Allows shapes, lines and freeform annotations to be drawn on proofs and for comment to be made on these marks..

How to use it

- Click on one of the shapes in the Drawing Markups section.
- Click on the proof at the relevant point and draw the selected shape with the cursor.
- To add a comment to the drawn shape, move the cursor over the shape until an arrowhead appears.
- Double click on the shape and type any text in the red box that appears.

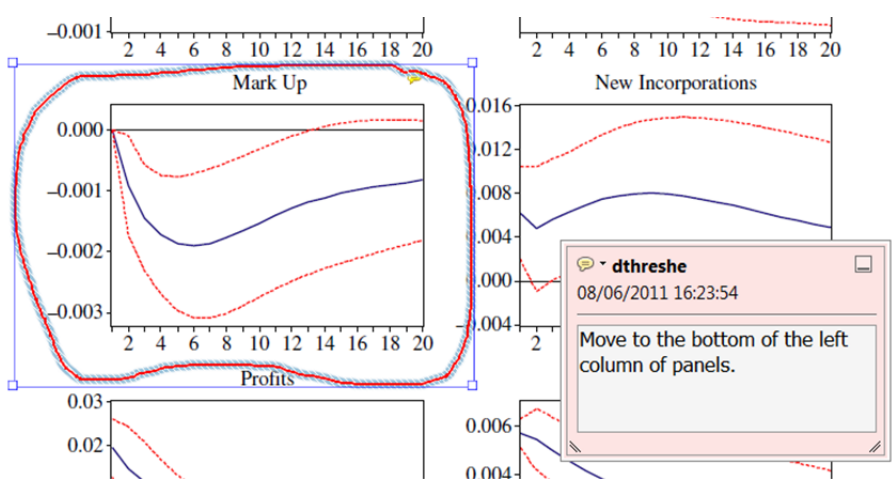

For further information on how to annotate proofs, click on the Help menu to reveal a list of further options: